ADVANCED OPTICAL MATERIALS
www.advopticalmat.de

Recent Advances in Flexible Inorganic Light Emitting Diodes: From Materials Design to Integrated Optoelectronic Platforms

*Hao Zhang and John A. Rogers**

The emergence of high-performance materials for flexible inorganic light emitting diodes (ILEDs) provides the foundations for a broad range of compelling, unconventional systems, from deformable displays and lighting sources to wearable and implantable bioelectronics with diagnostic and therapeutic capabilities. Interdisciplinary progress in materials synthetic methods, device designs, mechanical layouts, and assembly techniques over the past decade enables flexible ILEDs with remarkable operating characteristics even under extreme modes of mechanical deformation. This review summarizes recent advances in this field, with emphasis on the unique properties of the underlying materials and device physics in the first several sections. The subsequent content highlights examples of system-level integration of flexible ILEDs into advanced optoelectronic platforms with characteristics that would be difficult or impossible to achieve with conventional approaches. Miniaturized, implantable biomedical tools for optical modulation of neural activity at target sites and conformable, skin-mounted electronics for sensing and visualization of physiological parameters in real time provide examples of some of the most recent directions.

1. Introduction

Light emitting diodes (LEDs) are the enabling elements of the rapidly growing solid-state lighting industry. The most dominant LED technologies, widely used in residential general illumination, billboard displays, consumer electronics, and other applications, exploit epitaxial materials grown on rigid and planar substrates. These devices, in their conventional forms, cannot, however, flex, bend, or stretch in ways that are critically important for LED systems of the future, such as those for deformable displays,[1] electronic skins,[2] and bioinspired optoelectronics.[3] Organic molecules and polymers are natural choices for emitting materials in such classes of flexible LEDs, primarily due to their intrinsically low modulus, tunable and multicolor light emission, and their compatibility with roll-to-roll production on thin plastic substrates.[4] Despite significant progress over the past decades in organic LEDs (OLEDs), including many impressive demonstrations of flexible, high-resolution emissive displays, the performance degradation associated with photo-oxidation and/or other subtle processes necessitates the use of elaborate encapsulation schemes, even the most advanced of which have shortcomings in durability and lifetime particularly in humid environments. In addition, the limited spectral purity that follows from strong electron–phonon coupling in organic electroluminescent materials remains as a key challenge for OLEDs.[5]

By contrast, LEDs that rely on inorganic semiconductor emitting layers offer significant advantages over their organic counterparts in terms of electrical performance, such as lifetime, spectral purity, and brightness, and many require minimal encapsulation.[6] Research progress, especially over the last decade, in materials, device designs, fabrication concepts, and assembly approaches now provides a broad baseline of capabilities in inorganic light emitting diodes (ILEDs) that combine highly compliant mechanics with stable, robust high-performance operational characteristics. These emerging classes of flexible ILEDs can be categorized into two conceptually different but complementary approaches: i) ILEDs that follow from liftoff of micro/nanoscale semiconductor materials epitaxially grown on wafers and their deterministic assembly onto flexible target substrates with mechanically optimized interconnects; and ii) ILEDs that incorporate unusual active materials capable of direct, low temperature deposition onto thin plastic substrates. The first approach exploits well-established, high-performance III–V semiconductors processed in unusual ways, while the second leverages emerging classes of inorganic

Dr. H. Zhang
Department of Materials Science and Engineering
Northwestern University
Evanston, IL 60208, USA
Prof. J. A. Rogers
Departments of Materials Science and Engineering
Biomedical Engineering
Neurological Surgery
Chemistry
Mechanical Engineering
Electrical Engineering and Computer Science
Simpson Querrey Institute and Feinberg Medical School
Center for Bio-Integrated Electronics
Northwestern University
Evanston, IL 60208, USA
E-mail: jrogers@northwestern.edu
The ORCID identification number(s) for the author(s) of this article can be found under https://doi.org/10.1002/adom.201800936.

DOI: 10.1002/adom.201800936

semiconductors with rationally designed compositions and structures. Cointegration of either of these two classes of flexible ILEDs with other important electronic components creates new possibilities for advanced optoelectronic technologies, ranging from the next-generation displays in large or portable formats to wearable and implantable biomedical tools that conformally integrate with soft, curvilinear biointerfaces.

Other reviews on ILED technology focus on systems designed for use on rigid substrates.[5,7] The present paper highlights the most recent advances in flexible ILEDs, from the functional materials to state-of-the-art component-level and system-level embodiments. The content begins with sections on classes of inorganic emitters, including III–V epitaxial layers, colloidal quantum dots (QDs), metal halide-based perovskites, and 2D materials, for flexible ILEDs, from the perspective of the active materials and the device designs. A subsequent section presents the key ideas in system-level integration of state-of-the-art flexible ILEDs into advanced optoelectronic platforms for various applications, especially those in unconventional, biomedical tools for sensing, diagnosis, and therapy. Flexible ILEDs in wearable forms engineered to probe and visualize physiological information and in implantable platforms to modulate and measure neural activity represent some of the most advanced examples. A concluding section summarizes the current state of the field and discusses some challenges and directions for future work.

Hao Zhang is currently a postdoctoral researcher in the Department of Materials Science and Engineering at Northwestern University, Evanston, IL, working with Professor John A. Rogers. He received his B.S. and M.S. in chemistry at Tsinghua University in China in 2007 and 2010, and completed Ph.D. in Chemistry at University of Chicago in 2015. His research interests are surface chemistry of nanocrystal semiconductors and advanced optoelectronic devices for physiological monitoring and therapy.

John A. Rogers is the Louis Simpson and Kimberly Querrey Professor of Materials Science and Engineering, Biomedical Engineering and Neurological Surgery at Northwestern University. He obtained B.A. and B.S. degrees in physics from the University of Texas, Austin, in 1989, and completed his Ph.D. at Massachusetts Institute of Technology in 1995, studying physical chemistry. He was a faculty member at the University of Illinois at Urbana-Champaign from 2003, most recently as the Swanlund Chair Professor and Director of the Seitz Materials Research Laboratory. In 2016, he took his current position among the faculty at Northwestern University.

2. Flexible Micro-ILEDs (μ-ILEDs)

From a device-level perspective, III–V semiconductor based LEDs remain the most attractive candidates for solid-state lighting applications.[6,8] For instance, InGaN-based LEDs outperform many of other types of lighting modules, with high internal and external quantum efficiencies (IQE and EQE greater than 70% and 60%, respectively),[9] long lifetimes (>50 000 h vs <15 000 h for blue OLEDs),[10] and high luminous efficiencies (>200 lm W^{-1} compared to ≈90 lm W^{-1} of triphosphor fluorescent lamps).[11] Existing methods to utilize these ILEDs in commercial systems beyond simple modules for general illumination, such as billboard-scale displays, rely on sophisticated, robotic systems for high-throughput placement of thousands of individual devices onto a common platform. These processes typically involve multiple fabrication steps (wafer dicing, serial pick-and-place, (sub)millimeter scale packaging on a device-by-device basis, etc.) and collections of various components (e.g., bulk wires, lenses, and heat sinks).[1] Such methods cannot support assembly of ultrasmall (<200 μm × 200 μm, microscale), ultrathin (<50 μm) μ-ILEDs into addressable arrays with high spatial resolution, particularly on flexible substrates. A combined collection of recent strategies, from designs for μ-ILEDs epitaxially released in suspended configurations and still tethered to the underlying growth wafer, to methods for transfer printing of selected collections of these μ-ILEDs to target substrates, and schemes in planar registration of lithographically processed electrical interconnects based on conductors deposited by physical or chemical vapor deposition,[12] provide a solution to address these limitations and enable the use of μ-ILEDs in a wide range of previously unaddressed application possibilities.[1,13] This section reviews these and other recent developments in μ-ILED technologies with focus on materials designs, structural engineering, and assembly concepts.

2.1. Typical Fabrication Methods and Mechanical Designs for Flexible μ-ILEDs

The first demonstrations of flexible assemblies of μ-ILEDs involved red-emitting, epitaxial structures of high-performance III–V semiconductors.[1] Here, the epitaxial stack (**Figure 1**a) consists of AlInGaP quantum wells (6 nm thick $In_{0.56}Ga_{0.44}P$ wells, with 6 nm thick barriers of $Al_{0.25}Ga_{0.25}In_{0.5}P$ on top and bottom), cladding films, spreaders, and contacts, all deposited on GaAs source wafers with precise control over compositions and doping profiles. Isolated arrays of μ-ILEDs with microscale device layouts (e.g., 25 μm × 25 μm) follow from a combination of multiple photolithography and selective etching steps. Undercut etching of the sacrificial layer ($Al_{0.96}Ga_{0.04}As$ between

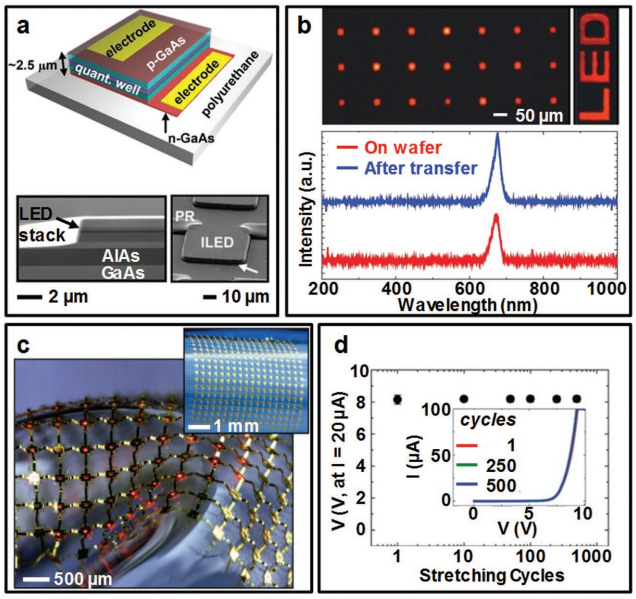

Figure 1. a) (Top) Schematic illustration of an AlGaInP μ-ILED with integrated Ohmic contacts on a flexible polyurethane substrate. (Bottom left) Cross-sectional scanning electron microscope (SEM) view of an AlGaInP μ-ILED, showing the semiconductor layers on a sacrificial epilayer of AlAs. (Bottom right) Angled-view SEM image of an individual μ-ILED. A pair of "breakaway" photoresist anchors at the two far corners of the device holds it above the GaAs wafer in a suspended configuration, for ease of liftoff with a stamp. b) (Top) Optical micrographs of an array of μ-ILEDs (Left: 25 μm × 25 μm, square geometries; Right: characters "LED") in the on state without illumination. (Bottom) Spectral characteristics of emission for a typical device on the wafer and after transfer printing. c) Photographs (main and inset) of a passive matrix, stretchable μ-ILED display that uses a noncoplanar mesh configuration, on a rubber substrate. d) Voltage needed to generate a current of 20 μA measured after stretching cycles to 500 times at an applied strain of 22%. The inset shows the current–voltage behavior after these cycling tests. Note that the three curves in the inset are coincident. Reproduced with permission.[1] Copyright 2009, The American Association for Advancement of Science.

the LED stack and GaAs source wafer) and photopatterning of "breakable" anchors of photoresist yield μ-ILEDs in suspended forms tethered to the underlying wafer at their corners (Figure 1a).[1,13i] Next, a fully automated printing tool lifts selected collections of μ-ILEDs (or "inks") from the source wafer and delivers them in organized arrays to a target, receiver substrate by use of a soft elastomeric stamp (typically made from polydimethylsiloxane (PDMS)) (Figure 1b, top panel). The μ-ILEDs prepared in this way preserve their electroluminescent characteristics relative to those processed in the conventional way on the growth substrates (Figure 1b, bottom panel). The assembly process, referred to as "transfer printing," exploits nonspecific van der Waals interactions between the solid inks and the relief structures on the stamps, along with schemes for reversibly switching the strength of this adhesion to facilitate retrieval and delivery. Advanced implementations of this technique enable deterministic assembly of μ-ILEDs with geometries that are orders of magnitude smaller and thus far more fragile, compared to existing (sub)millimeter scale ILEDs that can be manipulated by conventional pick-and-place methods, and with throughout speeds that are many orders of magnitude higher. Detailed descriptions of transfer printing and related techniques (e.g., sacrificial layers for undercut release, breakable photoresist anchors to tether inks, and adhesives to improve the yield of delivery[13h,14]) can be found elsewhere.[12a,c] Establishing interconnects (metals[1,13c,i] or graphene[15]) between the printed μ-ILEDs, in direct or matrix addressable patterns, completes the functional modules that can address requirements for a wide range of applications. The small thicknesses of μ-ILEDs (≈2.5 μm in initial demonstrations, and far thinner in more recent demonstrations) is a key feature that allows for facile interconnect definition and registration via standard, planar processing approaches, without the need for wire bonding.

Remarkable degrees of flexibility and deformability of modules that incorporate μ-ILEDs arise from their thin geometries, and from strategic mechanical designs at the system level. In this process, mechanics modeling and analysis provide guidance for layouts that minimize strains in the semiconductor stacks and other fragile electronic materials.[13e] For example, sandwiching the μ-ILED stack between two polymer layers (epoxy and polyurethane) with optimized thicknesses places the device near the neutral mechanical plane (NMP) where bending-induced strains are minimized. In extreme cases, in fact, the matched mechanical effects of the top and bottom polymer layers enable μ-ILEDs that can be bent to radii of curvature as small as 0.7 mm with negligible shifts in emission wavelength (≈1 nm) or intensity.[13b] In comparison, devices without the NMP layout show noticeable shifts in emission wavelengths (≈3.8 nm at a bending radius of 3.5 mm) associated with strain-induced changes in the bandgap.

Advanced geometric designs in the interconnects between μ-ILEDs can further enhance the levels of mechanical deformability.[12d,16] Other than the role of conducting components, the arc-shaped interconnects can also serve as structural bridges to accommodate significant strains (≈22%) by changes in their shapes, thereby allowing for stretchable μ-ILED displays on PDMS substrates (Figure 1c).[1] Typical flexible μ-ILED displays with this type of noncoplanar, mesh-shaped interconnects show no measurable changes in device performance such as current–voltage characteristics after up to a few hundreds of stretching cycles (Figure 1d).[1,12d,16] A combination of structurally engineered interconnects and NMP layouts offers μ-ILED systems with further improvements in flexibility (e.g., stretchability over 100%) and ability to deform in complex modes. **Figure 2**a shows an array of μ-ILEDs bridged by serpentine-shaped ribbons, where all functional materials lie near the NMP between two photodefined layers of epoxy.[13c] Transfer printing these interconnected μ-ILEDs to prestrained PDMS substrates with selective bonding sites, followed by strain release, yields noncoplanar serpentine interconnects via nonlinear buckling processes. These optimized mesh designs ensure unaltered performance at repeated, extreme deformational changes, such as uniaxial stretching to strains of 75% for 100 000 cycles. As predicted by mechanical modeling analysis, these μ-ILED arrays remain stable under complex, biaxial, shear, twisting, and other mixed distortional modes (Figure 2b,c).[13c] An example of a 6 × 6 array of μ-ILEDs pulled onto the sharp tip of a pencil experiences local strains as large as 100% but with invariant electrical/optical characteristics after up to 1000 cycles of deformation. The underlying mechanics, as revealed by quantitative

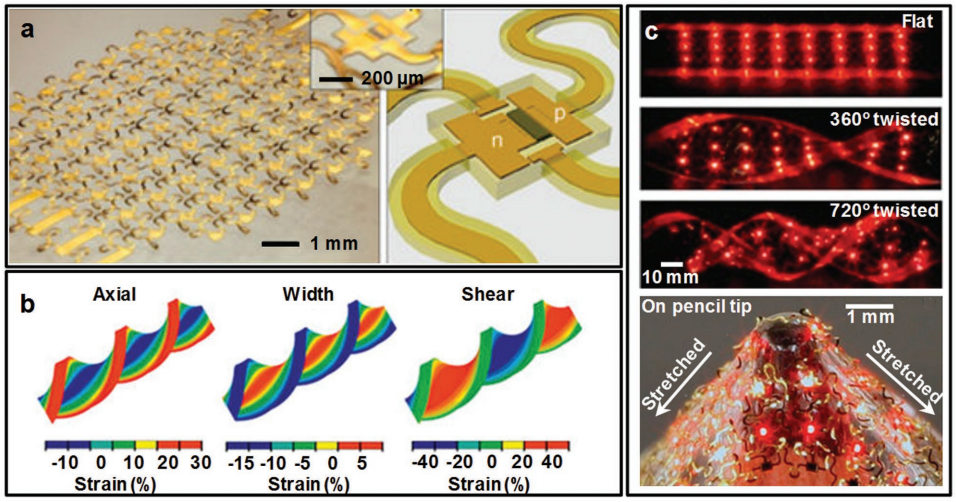

Figure 2. a) Optical image of a 6 × 6 array of μ-ILEDs (100 μm × 100 μm, and 2.5 μm thick, in an interconnected array with a pitch of ≈830 μm) with non-coplanar serpentine bridges on a thin (≈400 μm) PDMS substrate (left-hand frame). Schematic illustration (Right) and corresponding photograph (Inset) of a representative device, with encapsulation. b) Distributions of axial, width, and shear strain determined by 3D finite element modeling for twisting to 720°. c) (Top) Optical images of an array of μ-ILEDs (3 × 8) with serpentine interconnects on a band of PDMS twisted to different angles (0° (flat), 360°, and 720°); (Bottom) Optical image of an array of μ-ILEDs (6 × 6), tightly stretched on the sharp tip of a pencil, collected with external illumination. The white arrows indicate the direction of stretching. Reproduced with permission.[13c] Copyright 2010, Nature Publishing Group.

mechanical modeling, involves coordinated, in-plane and out-of-plane motions of the interconnects to accommodate strains associated with overall deformation, leaving the strains in the μ-ILED components within their linear elastic limit.[13c,15] Similar fabrication and design principles can be extended to stretchable μ-ILED arrays with graphene interconnects.[15] Low optical absorption, extremely low flexural rigidity, and serpentine layout designs in these graphene structures allow for highly transparent, μ-ILED arrays with reversible, linear elastic behavior at applied strains exceeding 100%. These optimized mechanical layouts enable intimate integration of μ-ILEDs with soft, curvilinear surfaces of human skin/internal organs and on nonplanar surgical tools (e.g., balloon-catheters) that involve significant changes in shape during operation, as highlighted in Section 6.[13c,d]

As mentioned above, the combination of high efficiency, bright electroluminescence, and long lifetime makes InGaN-based, blue-emitting LEDs among the most important candidates in energy efficient illumination modules.[11,17] Methods developed for red-emitting μ-ILEDs can also be adapted for InGaN-based μ-ILED assemblies in flexible formats.[13f-h,18] InGaN epitaxial stacks can be deposited on silicon[13f,19] or sapphire[13g,h,j,20] substrates with high levels of control over doping profiles. Separating photodefined μ-ILEDs from their growth wafers exploits either anisotropic wet etching[13f] or laser lift-off processes,[13g,h] depending on the choices of the growth wafers. The low cost and ready availability of large silicon wafer substrates are relevant, particularly because the silicon itself provides the basis for a simple release scheme via selective wet etching. Specifically, the release can exploit the large differences (>100 times) between the etching rates of Si (110) and Si (111) in hot, caustic baths of potassium hydroxide or tetramethylammonium hydroxide.[21] Anisotropic wet etching of epitaxial material grown on silicon wafers with (111) orientation yields μ-ILEDs in freely suspended configurations while tethered to source wafers via lithographically defined segments of InGaN (**Figure 3**a).[13f] Transfer printing methods enable high throughput, parallel delivery of millions of devices on flexible substrates with micrometer-scale position accuracy. In addition, the large bandgap of GaN (≈3.4 eV) offers a remarkably convenient means to define the contact regions for

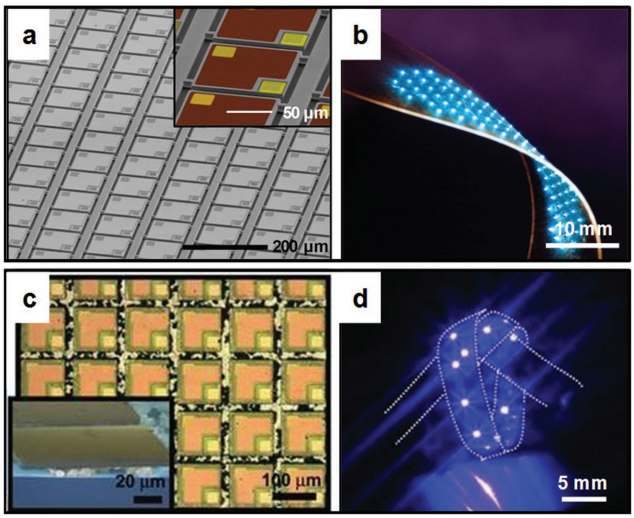

Figure 3. a) SEM image of a dense array of InGaN μ-ILEDs on a Si (111) wafer after an anisotropic etching process. Inset provides a magnified and colorized view. b) Optical image of a light module based on an array of μ-ILEDs on a plastic substrate. Reproduced with permission.[13f] Copyright 2011, The National Academy of Sciences. c) Optical microscope image and colorized, tilted view SEM image (inset) of GaN μ-ILEDs on sapphire substrates after an HCl etching process. Only isolated agglomerates of In–Pd alloys (black dots in the optical microscope image and pink structures in the SEM) remain. d) Arrays of GaN μ-ILEDs (12 devices) on a 4 mm × 15 mm strip of PET, tied into a knot to illustrate its deformability. Reproduced with permission.[13h] Copyright 2012, Wiley-VCH.

metal interconnects without the need for photomasking. Under a back-side exposure configuration, H-line UV light (≈405 nm) passes through the entire device except areas shadowed by the metal contacts. Washing away unexposed photoresist results in encapsulated devices with openings in the contact regions for the interconnect registration. These approaches allow for large area displays on flexible supports (Figure 3b) with densely packed μ-ILEDs (up to 396 μ-ILEDs over ≈12 cm^2).[13f]

Sapphire substrates are much more widely used than silicon wafers for growth of high quality, state-of-the-art blue-emitting epitaxial layers.[13h,22] Here, μ-ILED arrays with photodefined layouts can be bonded to a temporary silicon wafer by using In–Pd alloys for interfacial adhesion and then released from the sapphire via a laser lift-off process. Immersing the exposed μ-ILEDs into hydrochloric acid selectively removes the unalloyed indium to leave only alloyed agglomerates to tether the μ-ILEDs to the silicon (Figure 3c). A dual transfer printing process delivers selected collections of μ-ILEDs to target substrates such as polyethylene terephthalate (PET). These approaches enable flexible μ-ILED arrays with dimensions of each component ranging from 1 mm × 1 mm to 25 μm × 25 μm, limited only by the lithographic resolution, with excellent device performance (e.g., radiant efficiency up to ≈10%) even when strongly bent and twisted (Figure 3d).[13h]

2.2. Other Release Strategies and Fabrication Methods for Flexible μ-ILEDs

The fabrication techniques for the abovementioned and related systems of μ-ILEDs rely critically on transfer printing of lithographically defined μ-ILEDs released in thin form from their growth wafers to target, flexible substrates. The release of μ-ILED stacks from their source wafers by selective wet etching of the sacrificial layers followed from the schemes of epitaxial lift-off, first pioneered by Konagai et al. in 1978.[23] Advanced methods enable low cost production and high throughput creation of large quantities of high quality III–V materials as well as low dimensional semiconductors with favorable mechanical properties, both of which are promising candidates in cost-effective, flexible μ-ILEDs. **Figure 4** shows a scheme that exploits multilayer stacks in the release process, here shown with alternating GaAs (and/or AlGaAs) and AlAs layers grown on GaAs substrates.[13a] The compositions and layouts of the GaAs layers can be designed to satisfy specific application requirements. Immersion in hydrofluoric acid selectively etches the sacrificial AlAs layers and thus releases large quantities of GaAs. Transfer printing steps allow for sequential retrieval of individual device layers and their integration in various optoelectronic platforms. Compared to traditional single-layer lift-off approaches, this concept of multilayer release represents a more economically viable route, as it eliminates cycles of loading and unloading of wafers into the growth chambers and significantly reduces the rate of the degradation of growth wafers due to cycles of release. Selective wet etching of sacrificial layers can also enable the release of low dimensional III–V semiconductors with micro/nanostructures and their subsequent transfer to flexible substrates.[24] These low dimensional structures are formed by either top-down (e.g., selective etching) or bottom-up methods

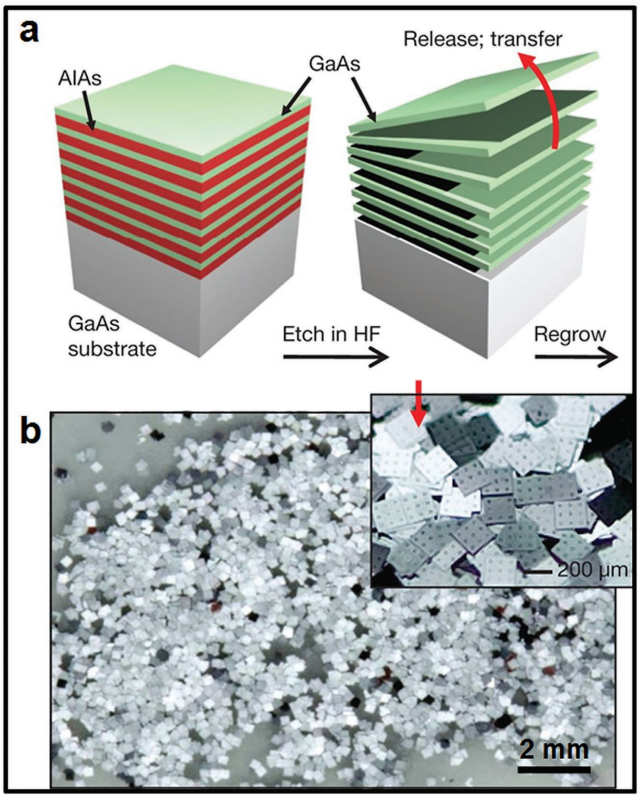

Figure 4. a) Schematic illustration of a multilayer stack of GaAs/AlAs and schemes for release through selective etching of the layers of AlAs. The GaAs substrates are reusable for additional growths. b) Optical image of a large collection of GaAs solar cells formed by release from a three-layer stack, and then solution casting onto another substrate. Inset in (b) show high-magnification view. Reproduced with permission.[13a] Copyright 2010, Nature Publishing Group.

(e.g., metal–organic chemical vapor deposition process) and show increased mechanical flexibility. For example, arrays of microdisks (7 μm diameter) containing InGaN/GaN multiple quantum wells are separated from the growth substrates by wet etching of SiO_2 sacrificial layers, followed by registration of metal contacts and interconnects on flexible substrates.[24a] The resulting blue-emitting GaN μ-ILEDs can accommodate extreme bending conditions (bending radii as small as 0.6–0.8 mm) and preserve over 70% of the electroluminescent intensity when bending radii are larger than 6 mm.

Intermediate layers such as 2D graphene enable the release of active semiconductor epilayers in the absence of sacrificial layers.[25] Coating a monolayer of graphene on top of GaAs (001) source wafers does not screen the mechanisms for epitaxial growth while the weak van der Waals forces of graphene allow rapid release of the grown epilayers by using metal stressors (**Figure 5**a).[25b] The exfoliated epilayers, after transferred to target substrates, perform as well as conventionally prepared materials, as highlighted in the case of AlGaInP-based ILEDs (Figure 5b,c). These remote epitaxial techniques and release schemes are general for various III–V materials, such as GaAs, InP, and GaP, and readily copy device-grade thin films from underlying wafers to substrates of interest. These features are of great relevance for advanced fabrication techniques

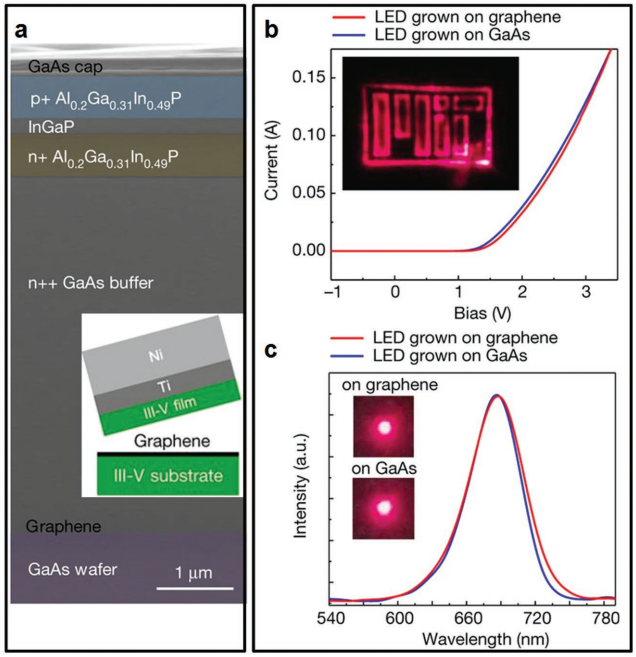

Figure 5. a) Cross-sectional SEM image of AlGaInP–GaInP double heterojunction LED stack grown on graphene-GaAs substrates. Inset illustrates the exfoliation of LED stacks from the growth substrates. b) Current–voltage curves of LEDs grown on graphene–GaAs substrates and directly on GaAs. Inset shows red light emission from the LEDs grown on the graphene–GaAs substrates. c) Electroluminescence spectra of the LEDs grown on graphene–GaAs substrates and directly on GaAs. Insets are the photos of functional LEDs. Reproduced with permission.[25b] Copyright 2017, Nature Publishing Group.

for flexible μ-ILEDs. Another representative example involves the mechanical lift-off of III–V nanowire arrays embedded in a PDMS matrix from growth wafers (sapphire) to flexible, target substrates.[26] Depending on the quantum well structures in nanowires, flexible ILEDs exhibit blue, green, and bicolor emissions with reliable operation after multiple (>10) bending cycles. Integrating down-converting phosphors to these blue-emitting nanowire ILEDs yields flexible white-emitting modules with EQE up to 9.3% and wall plug efficiency of 2.4%, showing no performance degradation when bent to a curvature radius of 5 mm.[26b]

The release of active III–V semiconductor layers can also be achieved by complete removal of the growth wafer.[27] As shown in **Figure 6**a, red-emitting AlGaInP epitaxial layers grown on GaAs wafers can be attached to thin polyimide (PI) films with preprinted bottom electrodes via anisotropic conductive film bonding.[27a] Wet etching with a mixture of ammonia water and hydrogen peroxide completely removes the GaAs wafer and exposes epitaxial structures for passivation and top interconnect definition. Flexible vertical μ-ILEDs on PI substrates made in this manner show almost identical electrical characteristics in their flat and bent states (bending radius ≈5 mm) (Figure 6b).[27a] The key challenges of this approach are that i) it consumes the entire source wafer and prevents its reuse for additional cycles of growth, and ii) μ-ILEDs on the source wafer and the final device share the same layouts and spatial distributions. These aspects limit design choices and cost-effectiveness in assembling μ-ILEDs, especially for systems that benefit from sparse arrays of μ-ILEDs, where a large areal ratio of the epitaxial material is unused.

2.3. Thermal Management of Flexible μ-ILEDs

Effective thermal management represents another important advantage of these flexible, interconnected μ-ILED arrays.[13f-h] Commercial, millimeter-scale LEDs require heat sinking structures to avoid significant increases in temperature and associated adverse thermal effects during operation.[28] Decreasing the sizes of the devices to the microscale regime leads to accelerated rates of thermal spreading due to favorable size scaling effects. Both simulation and experimental data reveal significantly reduced maximum temperatures (from ≈100 to ≈30 °C) during operation (with radiant intensity ≈160 mW mm^{-2}) as the sizes of μ-ILEDs decrease by a factor of 1600 from 1 mm × 1 mm to 25 μm × 25 μm.[13h] Moreover, in this small size regime, the metals interconnect themselves, due to their thermal mass and thermal conductivity, serve concurrently as effective heat sinks.[13f] A combination of geometrical designs (sizes of μ-ILEDs, thicknesses, and widths of interconnects) and advanced electronic strategies (pulsed operation with various duty cycles) enables stable operation as well as controllable thermal behaviors of μ-ILEDs, even when wirelessly powered with integrated metal inductor coils and supported by plastic substrates with modest thermal budgets.[13g]

Following from advances in epitaxial release, deterministic assembly techniques, structural design concepts, and thermal control strategies, flexible μ-ILEDs are now promising candidates

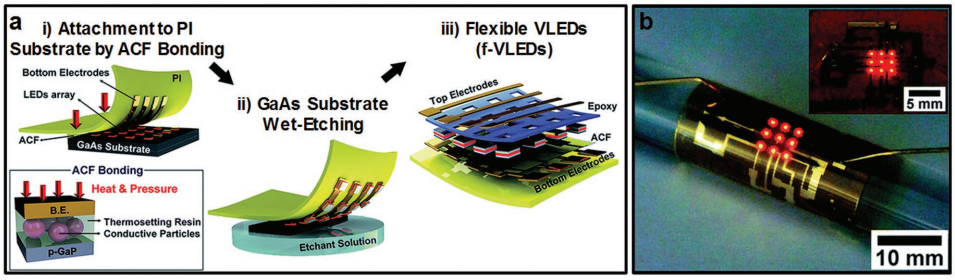

Figure 6. a) Illustrations of the steps for fabricating an array of red-emitting AlGaInP flexible vertical LEDs with multiquantum well layers. b) Photographs of a 3 × 3 array of flexible vertical LEDs in a bent state on a glass rod (radius of curvature = 5 mm) and in a flat state (inset). Reproduced with permission.[27a] Copyright 2014, The Royal Society of Chemistry.

in emerging applications that are otherwise inaccessible with conventional ILEDs, ranging from high-resolution deformable displays to lighting modules seamlessly integrated with soft, curvilinear surfaces of skin and other biotissues for physiological sensing, neural activity modulation, and clinical therapy. Some representative examples appear in Section 6.

3. Flexible Quantum Dot LEDs (QLEDs)

Recent progress in flexible ILEDs also follows from developments in unconventional inorganic emitting materials and advances in understanding their unusual optoelectronic behaviors. Though still inferior to conventional III–V semiconductors from the device standpoint, these new materials, as will be presented in Sections 3–5, offer intriguing routes to flexible ILEDs, with versatile control over optical properties, ultrahigh color purity and extended color gamut, ultrathin profiles, and excellent solution processability and associated compatibility with flexible substrates.

Among these materials, colloidal inorganic semiconductor QDs are arguably the most promising candidates in flexible ILEDs. The most valuable attributes of QDs are their broad spectral tunability from UV to near IR (NIR) and narrow emission peaks with full-width at half-maximum (FWHM) of ≈30 nm, which are difficult to achieve by OLEDs or conventional down-converting phosphors. Additionally, as with organic species, QDs in their colloidal forms are amenable to broad sets of solution-based fabrication techniques, with promise in low cost, large scale assembly into solid-state devices.[7b,29] Systems that harness this unique combination of properties now include commercial display technologies, such as Samsung Quantum Dot TVs and Amazon Kindle Fire HDX 7 Tablets.[30] Significant efforts toward the development of electroluminescent QLEDs have been made since their first appearance more than two decades ago,[31] as summarized in several recent reviews.[5,7b,32] This section begins with a brief introduction of the intriguing optoelectronic properties of QDs enabled by precise synthetic control and proper structural engineering and then focuses on the most recent advances in flexible QLEDs, especially those for highly pixel count, stretchable displays.

3.1. Optical Properties of QDs

Established synthetic methodologies, especially those reliant on the pyrolysis of molecular precursors in hot organic solvents, yield QDs with various sizes, compositions, shapes, as well as surface chemistries in a controllable manner.[29] These versatile chemistries and their ability for precise control over compositions and structures provide access to QDs with remarkable and readily tunable emission properties. i) Spectral tunability. The sizes of QDs are typically within the range of 2–20 nm, where quantum confinement leads to discrete electronic states, and the well-known size-dependent bandgaps and emission wavelengths.[36] For example, cadmium selenide (CdSe) QDs with increasing sizes exhibit emission colors from blue to red (**Figure 7**a).[33,36c,37] As with conventional semiconductors, spectral tunability also arises from QD composition. The complementary controls provided by size and composition enable emissions from CdSe- and PbS-based QDs that cover the entire visible and a large fraction of NIR spectrum (Figure 7b).[7b] Efficient NIR emission and spectral tunability afforded by IV–VI,[38] III–V,[39] and other QDs represent a distinct advantage over organic emitters. ii) Color purity. The color purity, or spectral linewidth, of QD ensembles depends on both the averaged emission spectra of individual QDs (homogeneous broadening) and variations in emission spectra of all QDs in these ensembles

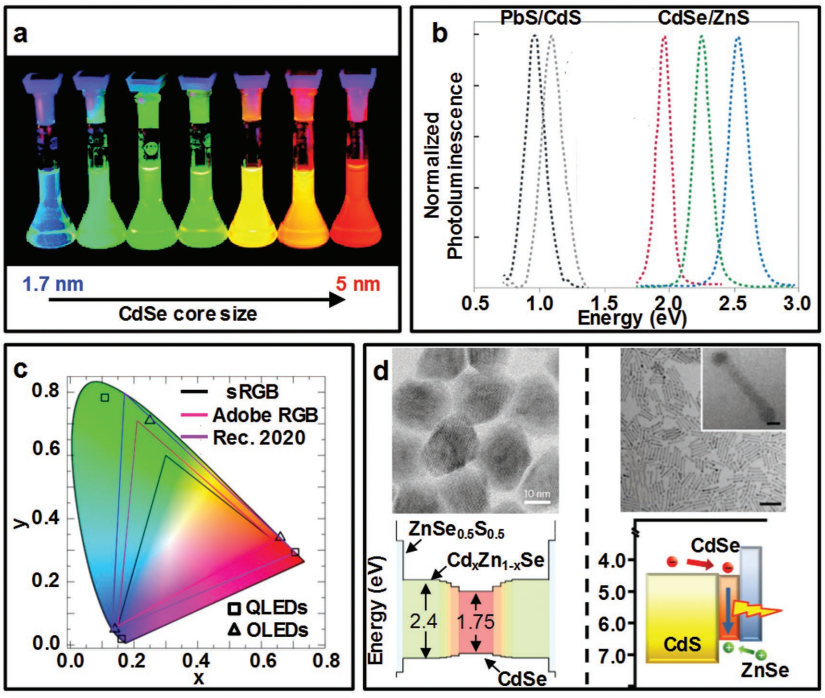

Figure 7. a) Size-dependent change of the emission color for colloidal solutions of CdSe/ZnS core–shell QDs. Reproduced with permission.[33] Copyright 2002, Wiley-VCH. b) PL spectra of CdSe/ZnS and PbS/CdS core/shell colloidal QDs, demonstrating the size- and composition-dependent tunability of QD emission color. Reproduced with permission.[7b] Copyright 2013, Nature Publishing Group. c) Representative RGB color spaces (solid lines) and chromaticity points of RGB QLEDs (squares) and cutting-edge OLED products (triangles) relative to the CIE 1931 chromaticity diagram. While state-of-the-art OLEDs can only cover sRGB or Adobe RGB color space with advanced optical engineering, QLEDs easily meet the current standards and satisfy Rec. 2020. Reproduced with permission.[5] Copyright 2016, American Chemical Society. d) Band engineering of QDs that involve heterostructures. (Left) Representative transmission electron microscope (TEM) images and band structures of core/shell (continuously graded CdSe/$Cd_xZn_{1-x}Se$/$ZnSe_{0.5}S_{0.5}$) QDs. Reproduced with permission.[34] Copyright 2018, Nature Publishing Group. (Right) Representative TEM image and band structures of DHNRs. Scale bars in the TEM image and the inset: 50 and 5 nm. Reproduced with permission.[35] Copyright 2014, Nature Publishing Group.

(inhomogeneous broadening).[40] For high-quality ensembles of monodisperse QDs (size distribution within 5%), the spectral linewidth approaches those of individual QDs (FWHM ≈ 20 nm). In comparison, emission from OLEDs is limited by strong electron–phonon coupling, with multiple and significantly broadened peaks (FWHM: 40–60 nm). High color purity, together with continuously tunable spectrum, allows for QLEDs with a color gamut that satisfies the Rec. 2020 standard for ultrahigh definition TV (Figure 7c).[5,7b,32a] iii) Brightness. Facile injection/extraction of charge carriers/photons and high light emission quantum yield (defined as the ratio of radiative recombination rate to the sum of rates of radiative and nonradiative recombination) are prerequisites for high EQE and brightness. Advanced synthetic methods yield QD heterostructures that are favorable for these processes and improved EQEs (Figure 7d). QDs with core–shell structures minimize nonradiative carrier recombination by physical separation of electron–hole pairs in the core (typically CdSe) from surface defects on the shell (CdS, ZnS, or their alloys) and they suppress Auger processes (with an alloyed shell).[34,41] With optimized surface chemistry, core–shell QDs show near unity photoluminescent (PL) quantum efficiency and represent the preferred choices for QLEDs, especially for commercialized products.[42] Structurally sophisticated double heterojunction nanorods (DHNRs) comprise two wide bandgap semiconductors (CdS and ZnSe) with type II band offset surrounding and in contact with a narrow bandgap (CdSe) emitting center.[35,43] The staggered band offset between CdS and ZnSe in the energy diagram allows for efficient injection of both electrons and holes while the anisotropic optical properties result in increases in the upper limit of light outcoupling.[43a] Both effects enhance EQEs. Detailed discussions of band engineering in heterostructured QDs and underlying physical behaviors can be found in a recent review.[5] These attractive optical properties follow from advanced synthetic strategies that are critically important to the progress of QLEDs. When fabricated on regular, rigid substrates, device performance of QLEDs compare well with state-of-the-art OLEDs (record EQEs and brightnesses for QLEDs: red: 20.5%,[44] 106 000 cd m^{-2}[45]; green: 15.6%,[46] 218 800 cd m^{-2}[47]; blue: 10.7%,[48] 7600 cd m^{-2}[48b]).

3.2. Advanced Patterning Techniques for QLEDs

Advanced patterning and fabrication techniques allow for high-performance flexible QLEDs. Spin-coating and related solution-based casting techniques are effective in preparing electroluminescent QD monolayers in QLEDs, especially those with monochromic emission. However, issues such as cross-contamination and redissolution of QDs during sequential spin-coating processes and inevitable energy transfer between QDs of different colors limit the use of these techniques in highly pixelated, full-color QLED displays or lighting devices. Transfer printing techniques, similar to those described for μ-ILEDs, circumvent these problems and offer powerful methods to generate precisely patterned QD pixels.[41b,49] Early demonstrations of transfer printing QD films involved spin-coating thin layers of QDs on PDMS stamps chemically modified for solvent compatibility.[49d] Later iterations involve the use of the stamps to retrieve QDs from selected regions of thin films formed on "donor" substrates, for subsequent delivery to target substrates in a deterministic, parallel fashion.[49a,50] This solvent-free, sequential transfer printing process allows scaled production of sophisticated displays, including a demonstration of a 4 inch full-color display with 320 × 240 QD RGB (red, green, blue) pixels, each with a dimension of 46 μm × 96 μm.[50] During the "inking" process, the stresses and cracking behaviors in the QD layers are more complex than those associated with tethered μ-ILEDs. As a consequence, discrepancies between designed and printed patterns of QDs can occur for high-resolution geometries, particularly with pixel sizes below 35 μm.[49b] An additional contact to a substrate with intaglio trenches followed by slow detachment ensures that cracks only form at the edges of the trenches, leaving noncontacted regions of the QD films with sharp edges on the stamps. A subsequent contact printing step delivers highly uniform, ultrasmall QD pixels (as small as 5 μm) to virtually any substrate (**Figure 8**a). This intaglio transfer printing process offers high fidelity and printing yields approaching 100%, for full-color QD displays with ultrahigh resolution (2460 pixels per inch, p.p.i.).[49b]

In addition to the QD layers, transfer printing methods can apply to multilayer stacks that include the QD emitting layers, charge transport layers, conductive electrodes, and even substrate

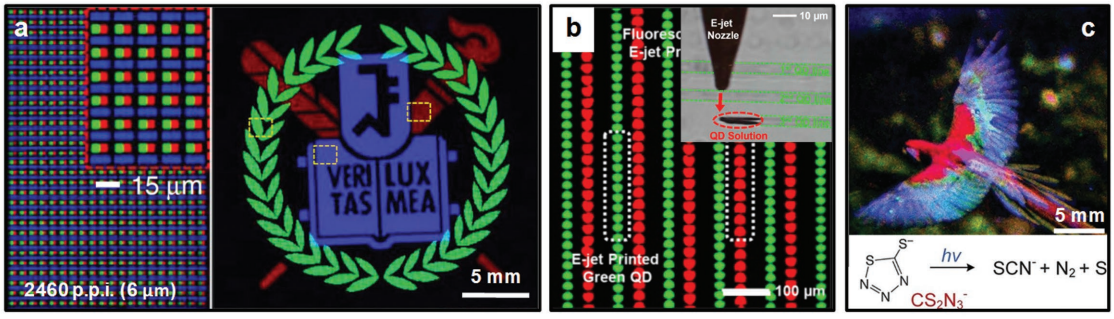

Figure 8. a) Intaglio transfer printing for high-resolution RGB QLEDs. (Left) A PL image showing aligned RGB pixels (2460 p.p.i. with the pixel size of 6 μm). (Right) A PL image of RGB QD patterns via multiple aligned steps in transfer printing. Reproduced under the terms of CC BY 4.0 license.[49b] Copyright 2015, The Authors, published by Nature Publishing Group. b) Composite fluorescence images of dual color QD patterns formed by electrohydrodynamic jet (e-jet) printing. Inset shows an optical microscope image of a metal-coated glass nozzle (5 μm inner diameter at the tip) and a target substrate during e-jet printing. Reproduced with permission.[51] Copyright 2015, American Chemical Society. c) (Top) A true-color image containing ≈8×10^5 RGB subpixels directly photopatterned by use of $CS_2N_3^-$-capped QDs via the DOLFIN process. (Bottom) Chemical reaction for the photodecomposition of $CS_2N_3^-$ ligands. Reproduced with permission.[52] Copyright 2017, The American Association for Advancement of Science.

layers.[49c,53] By using a sacrificial fluoropolymer to provide low energy surfaces for release, this type of multilayer transfer printing process allows the incorporation of red- and green-emitting QD assemblies with different, optimized electron transport layers (ZnO and TiO_2) and the same hole transport/anode layers.[49c] The independently tailored band alignments between green QDs/TiO_2 and red QDs/ZnO and well-matched highest occupied molecular orbitals (HOMO)/lowest unoccupied molecular orbitals (LUMO) levels result in improved charge carrier injection efficiencies and accordingly higher EQEs. Furthermore, the capability for transfer printing the entire QLED stack to prestrained elastomeric substrates yields fully stretchable, wavy QLED arrays through buckling processes.[53] The bending radii in such systems can be as small as 35 μm without mechanical damage or electrical degradation.

Besides dry processing approaches based on contact printing, solution-based techniques such as hydrodynamic inkjet printing[51,54] and 3D printing[55] provide viable routes to high-resolution QLEDs. Under optimized conditions (printing nozzle sizes, QD ink formula, applied voltages, etc.), inkjet printing offers capabilities for fully programmable, sequential patterning of QDs with different colors into elaborate patterns, and with nanoscale control over the thicknesses and lateral dimensions (Figure 8b).[51] A distinct advantage of inkjet and 3D printing methods over contact printing or spin-coating techniques is their ability to conformally print components on nonplanar, complex surfaces. As a proof-of-concept, emissive QDs, polymeric charge transport layers, metal contacts, substrate, and encapsulation layers can be 3D-printed onto contact lenses, resulting in QLEDs with 3D freedom in design.[55]

Direct photopatterning of inorganic nanomaterials enabled by rationally designed surface ligands represents an alternative, facile approach toward high-resolution pixels in QLED displays. This method, termed as DOLFIN (direct optical lithography for inorganic nanomaterials), exploits photoinduced solubility changes of various types of nanocrystals (including QDs) functionalized with photosensitive ligands, such as 1,2,3,4-thiatriazole-5-thiolate (Figure 8c).[52] Using conventional mask aligners and photomasks, spin-coated thin films of QDs in UV-exposed or unexposed regions can be washed away depending on the types of surface ligands, thereby allowing for a photoresist-free photolithographic approach to patterning. Implementing DOLFIN with QDs of red, green, and blue colors yields large area, pixelated (0.8 million RGB subpixels in an area of ≈2 cm × 2 cm) patterns with high resolution in both the lateral (1 μm, determined by mask resolution) and vertical (10 nm accuracy) directions. Compared to traditional photolithography with photoresist, DOLFIN requires far fewer fabrication steps in patterning multiple layers of the same or different materials and it circumvents adverse effects of organic impurities in charge carrier injection/transport in QD assemblies. Moreover, the DOLFIN processes are mainly based on low temperature, solution techniques, which are fully compatible with flexible substrates.

3.3. Representative Examples of High-Performance, Flexible QLEDs

Rational materials design and advanced assembly techniques set the basis for device-level and system-level embodiments of flexible QLEDs, especially their incorporation into advanced optoelectronic platforms such as next generation displays and skin-mounted, biocompatible modules for monitoring and visualization of physiological information. Adapted from OLEDs and QLEDs originally designed for use on rigid substrates, optimized device architectures for flexible QLEDs (**Figure 9**a) feature an ultrathin emissive layer of core–shell QDs, sandwiched between hybrid charge transport layers, typically the inorganic electron transporter based on sol–gel TiO_2 or ZnO nanoparticles and the organic hole transporting polymer such as poly[(9,9-dioctylfluorenyl-2,7-diyl)-co-(4,4′-(N-(4-sec-butylphenyl))diphenylamine)] (TFB).[49a,b,50,56] These choices of charge transport layers follow from consideration of balanced electron/hole injection rates and their processing compatibility with flexible substrates. The first demonstration of large area, full-color flexible QLEDs utilized transfer-printed RGB pixels composed of II–VI core–shell QDs on polyethylene naphthalate (PEN) substrates (Figure 9b).[50] Mechanical tests show no degradation in luminous efficiency or current–voltage characteristics at bending radii of 3 cm. Flexible white QLEDs exploit similar device structures but different strategies in mixing RGB QDs to realize white emission. Active layers with homogeneously mixed QDs (dichromic to tetrachromic)[57] or sequentially stacked RGB layers[49a] suffer from inevitable inter-QD energy transfer and sophisticated control of contents of QDs of different colors. Sequential intaglio transfer printing steps yield flexible white QLEDs with aligned RGB pixels and true white color emission with CIE coordinates of (0.39, 0.38) (Figure 9c).[49b] Compared to white QLEDs with mixed QDs in emitting layers, pixelated devices show improved EQE (up to 1.5%) across the entire operating range and enhanced brightness (10–52%) depending on applied voltages. At different bending angles (up to 135°, Figure 9d), these flexible QLEDs remain stable with no changes in current–voltage characteristics.

Optimizing the device architectures, QD heterostructures, and substrate/encapsulation materials leads to improved electrical and mechanical performance. Green-emitting QLEDs with an inverted architecture exhibit unprecedently high EQE (15.6%) and current efficiency (65.3 cd A^{-1}).[46] Of particular importance in this design is the interfacial layer of polyethylenimine ethoxylated that lies between the QD emitting layer and the polymer hole transport layer, to prevent damage during sequential deposition of these two layers and also to upshift the HOMO level of QDs for improved hole injection. Flexible inverted QLEDs with a similar structure also show high performance with a maximum EQE of 8.4% and a current efficiency of 35.1 cd A^{-1}, both among the highest values reported for flexible QLEDs.[46] These all-solution processed flexible QLEDs also exhibit good mechanical properties and remain operational in highly bent states. Structural engineering of QDs offers another route to improved device performance. Green-emitting QDs with relatively thick shells (2 nm thicker compared to conventional core/shell QDs) show drastically suppressed nonradiative, Auger recombination, and prolonged PL lifetime. Consequently, flexible QLEDs using QDs with thicker shells show luminous efficiency that are 10 times higher than those with conventional QDs and a brightness of 44 719 cd m^{-2} at 9 V, also among the highest reported values for flexible QLEDs.[56c] In terms of mechanics, early examples of flexible QLED devices

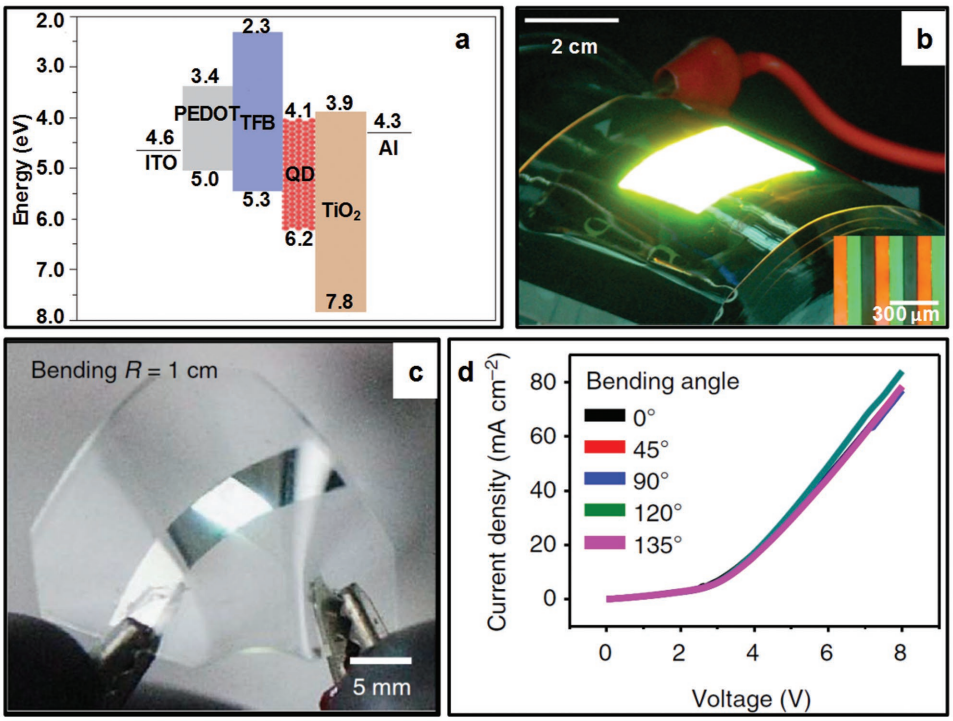

Figure 9. a) A typical device structure and energy band diagram of flexible QLEDs that use inorganic/organic hybrid charge transporting layers. b) Flexible full-color QLED with RGB pixels patterned by transfer printing onto a PEN substrate. Inset: optical image of simultaneous electroluminescence emission of RGB patterned QDs. Reproduced with permission.[50] Copyright 2011, Nature Publishing Group. c) Optical image of flexible white QLEDs with Intaglio transfer printed RGB QD pixels. The bending radius is 1 cm. d) Electrical properties (current–voltage characteristics) of flexible white QLEDs at different bending angles. Reproduced under the terms of the CC BY 4.0 license.[49b] Copyright 2015, The Authors, published by Nature Publishing Group.

could bend to some extent (minimum bending radii of several tens of millimeters[32a]) but they could not undergo more complex mechanical deformations. The limited flexibility mostly originates from the large thicknesses of the plastic substrates (e.g., several hundreds of micrometers for PET[46]) and the brittle nature of commonly used indium tin oxide (ITO) electrodes. Using thin polyimide (Kapton) tapes as substrates and thin metallic films as electrodes allows for highly flexible and mechanically robust QLEDs with high EQEs for different emission colors (≈4% for red and green and ≈1% for blue).[58] The devices preserve about 87.5% of the initial brightness (20 000 cd m^{-2}) after 500 cycles of bending on a 4 mm diameter rod. Such devices can be used as stickers for mounting on curved surfaces of 3D objects. Further reductions in substrate thickness to the micrometer scale and integration with elastomeric supports yield stretchable QLEDs capable of complex modes of deformation and conformal integration with soft, curvilinear surfaces. Here, the ultrathin substrates (≈1.1 µm) consist of parylene and epoxy layers and concurrently serve as biocompatible, water-proof encapsulation materials.[49b] Placing QDs and other active layers (especially ITO) between two substrate/encapsulation layers (near NMP) yields ultrathin (total thickness about 2.6 µm), tattoo-like QLEDs that can be bent, stretched, folded, or crumped (**Figure 10**a,b). These QLED tattoos exhibit high EQEs over a wide range of applied voltages (over 1% at 3.6–6.9 V with the maximum value of 2.35% at 4.5 V) and a high brightness of 14 000 cd m^{-2} at 7 V. These values remain unchanged after 1000 cycles of uniaxial stretching to strains of 20% (Figure 10c).[49b]

These collective advances in flexible QLEDs follow from interdisciplinary research in synthetic chemistry, quantum physics, optoelectronic materials, and mechanical engineering, and yield interesting opportunities in emerging display technologies and skin-mounted electronics. Representative examples for such applications[53,56b,c,59] appear in Section 6.

4. Flexible Perovskite LEDs (PeLEDs)

4.1. Optical Properties of Metal Halide-Based Perovskites

Metal halide-based perovskites are an old class of material. Those based on lead halides (with ABX_3 crystal structures, where A is a monovalent alkali metal or organic cation, B is Pb, and X are halide anions or their mixtures) in particular are of increasing interest in the last several years, primarily due to their promising performance in photovoltaic cells.[60] The high power conversion efficiencies in such cases (certified value of 23.3%[61]) also suggest the potential use of perovskites as emitting materials in LEDs, according to the Shockley–Queisser detailed balance limit calculations.[7c,62] As with QDs, perovskites feature both widely tunable emission spectra and exceptionally high color purity. The color tunability of lead halide perovskites follows mostly from changes

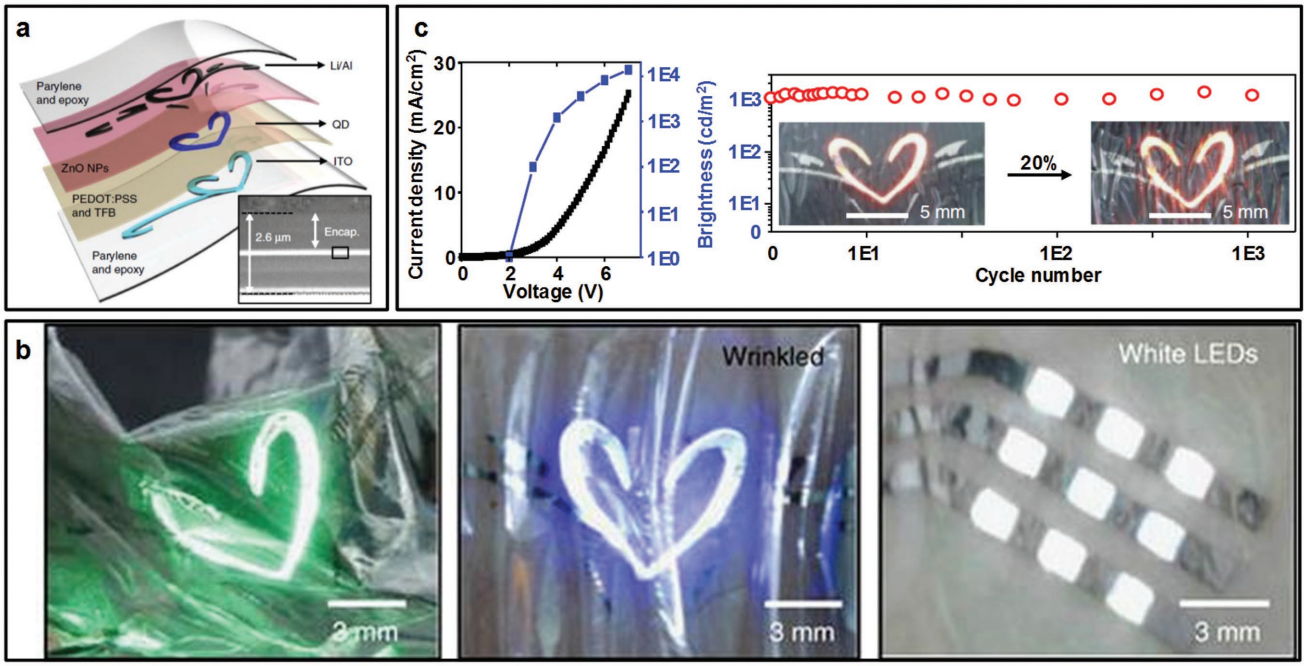

Figure 10. a) Exploded view illustration of an ultrathin, tattoo-like wearable QLED. Inset shows a cross-sectional SEM image in which the thickness of the encapsulation and active layers are shown. b) (From left to right) Optical images of ultrathin green QLEDs laminated on crumpled Al foil, blue QLEDs laminated on skin, and wearable white QLED arrays laminated on skin. c) (Left) Current density–voltage–luminance characteristics of the ultrathin, wearable QLEDs shown in (a). (Right) Stable brightness in multiple stretching experiments (20%, 1000 times). The inset shows photographs of buckled and stretched ultrathin red QLEDs. Reproduced under the terms of the CC BY 4.0 license.[49b] Copyright 2015, The Authors, published by Nature Publishing Group.

in compositions. For example, tuning ratios of different halide anions yield perovskites that can emit across a broad range from 390 to 820 nm (**Figure 11**a).[7a] Quantum effects of perovskites with sizes in the confinement regime provide means for additional, improved control over the bandgaps and emission wavelengths. Unlike QDs, perovskites have intrinsically narrow emission linewidths (FWHM as small as ≈20 nm) regardless of grain size. This behavior originates from their structural similarity to multiple quantum wells.[63] These spectral features lead to a well-extended color gamut, as shown in Figure 11b. In addition, owing to the highly ionic nature of metal–halogen bonds, perovskites with various sizes and in different forms are readily available, from nanoscale materials (sub-10 nm QDs,[64] nanowires,[65] and 2D nanoplatelets[66]), to polycrystalline grains (sub-100 nm to millimeters),[67] and to millimeter-scale, single crystals with low defect densities.[68] In many cases, high quality perovskite structures can be synthesized and processed by using solution-based methods at low temperatures that are compatible with flexible, plastic substrates.[64a] All of these attributes make perovskites attractive, alternative choices for high-performance LEDs. Following from design concepts and fabrication techniques previously used for conventional LEDs and perovskite photovoltaics, PeLEDs with EQEs exceeding 10% in green, red, and NIR regions can be achieved on rigid substrates.[69] These values are impressive considering the short history of modern PeLEDs.[63a] Progress related to material design and device performance of PeLEDs on conventional, rigid substrates appears in several recent reviews.[7a,c,67a] This section highlights recent advances in flexible PeLEDs on plastic substrates.

4.2. Representative Examples of High-Performance, Flexible PeLEDs

The first examples of high-performance PeLEDs employed a simple bilayer structure with methylammonium lead bromide ($MAPbBr_3$) perovskites as the emitting layer and 2,2′,2″-(1,3,5-benzinetriyl)-tris(1-phenyl-1-H-benzimidazole) (TPBI) as the electron transport layer (**Figure 12**a).[70] In this structure, LiF/Al and a self-organized conducting polymer serve as cathode and anode, respectively. Green-emitting PeLEDs using this device architecture and fabricated on glass substrates have an EQE of ≈8.53% (≈10 times higher than EQEs in visible PeLEDs reported prior to this work) and a current efficiency of 42.9 cd A^{-1}. Such improvements in device performance follow from both compositional control and grain engineering of the emitting layers. On the one hand, a slight excess of MABr in the synthesis (10% higher than the stoichiometric ratio) prevents the formation of metallic Pb defects that potentially quench excitons and decrease the ionization energy of $MAPbBr_3$ for more efficient charge injection. On the other hand, the intrinsically long carrier diffusion lengths (≈1 μm) and low exciton binding energies (tens of millielectron volts) of perovskite crystals[71] can lead to substantial leakage currents and corresponding reductions in current efficiencies.[63a,70] Use of a nanocrystal pinning process and TPBI additives significantly reduces the grain sizes of $MAPbBr_3$ from several micrometers to ≈100 nm (Figure 12b). These uniform, small grains lead to strong spatial confinement of excitons (the carrier diffusion length is ≈67 nm) and thereby reduce nonradiative

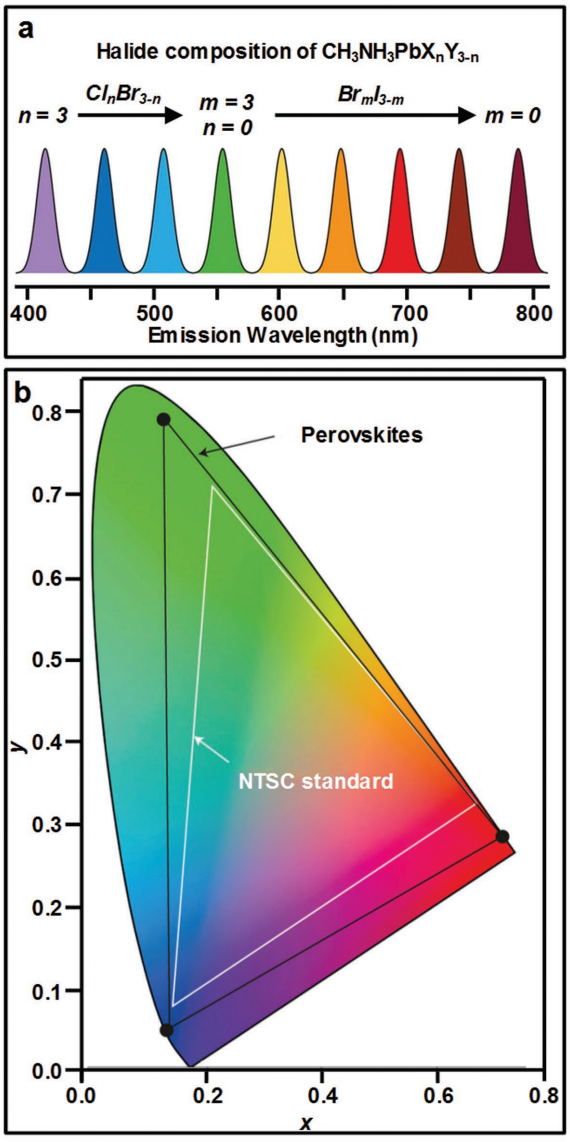

Figure 11. a) Emission-wavelength tunability of $CH_3NH_3PbX_nY_{3-n}$. The emission of the $CH_3NH_3PbX_nY_{3-n}$ perovskite is tunable from wavelengths of 390–790 nm. b) CIE chromaticity diagram. Perovskites have color spaces that cover an area larger than the National Television System Committee (NTSC) standard. Reproduced with permission.[7a] Copyright 2016, Nature Publishing Group.

recombination. Flexible PeLEDs on PET substrates based on the same emitting materials with precise control over compositions and grain sizes show high brightness, robust operation even at highly bent states (Figure 12c). Besides conducting polymers, graphene can be used as an anode material. Flexible PeLEDs with $MAPbBr_3$ nanograins (≈26.7 nm), a buffer hole-injection layer, and graphene anodes show current efficiencies of 16.1 cd A^{-1} and maximum brightness of 13 000 cd m^{-2} (Figure 12d).[72] When fabricated on 200 µm thick PET substrates with four layers of graphene as anodes, these PeLEDs can endure 5.3% tensile strain at a bending radius of 1.9 mm without notable changes in current densities (Figure 12e). Over 80% of the initial current density remains after 1200 cycles of repeated bending events (bending radius of 200 µm with 1.34% strain, Figure 12f). By comparison, PeLEDs using brittle ITO for the anodes degrade significantly after 200 bending cycles and completely fail after 1200 cycles.

Nanoscale perovskite materials with size scales in the quantum confined regime represent a promising class of materials for photonic sources.[7a,64] Syntheses of perovskite QDs, nanowires, or quantum wells are possible via simple colloidal approaches, and in some cases, even in open beakers and at room temperatures.[64a] These versatile chemistries yield nanoscale perovskites with precisely controllable sizes and shapes and improved optical properties. For example, perovskite QDs possess ultrasmall sizes and significantly larger exciton binding energies than their bulk counterparts, which can promote radiative recombination by confining excitons to nanoscale regions. Moreover, quantum confinement offers an additional degree of freedom in fine-tuning of the size dependent optical properties and enables flexible PeLEDs with unprecedented color purity and wide gamut. 2D perovskite quantum wells of $FAPbBr_3$ (FA: formamidinium) perovskites with well-controlled sizes and compositions exhibit an ultrapure green emission at 529 nm with a linewidth of only ≈20 nm and a PL efficiency of ≈90% (**Figure 13**a).[73] The PL efficiency of these 2D quantum wells approaches ≈92% in the solid state, which is among the highest reported value for all perovskite thin films. These attributes enable PeLEDs with the purest green emission ever achieved, which covers 97% and 99% of the Rec. 2020 standard in the CIE 1931 and CIE 1976. Flexible PeLEDs made on thin PI substrates (50 µm) can be bent to radii as small as 2 mm (bending radius of 7.5 mm shown in Figure 13a) with invariant emission spectra. A more recent embodiment of flexible PeLEDs harnesses self-assembled $CsPbBr_3$ supercrystals (SCs) from ≈10 nm cubic building blocks (Figure 13b).[74] These SCs exhibit even "greener" emission with color coordinates closer to the edges of the spectral locus of Rec. 2020 compared to those of previously reported $FAPbBr_3$ quantum wells (Figure 13c). These results highlight the promising applications of flexible PeLEDs as light sources that can outperform other types of LEDs in terms of color purity. In addition, thin films made from sub-10 nm perovskite QDs also show higher mechanical robustness compared to polycrystalline perovskites.[75] Flexible PeLEDs with ≈7 nm $MAPbBr_3$ QDs can endure 1000 cycles of repeated bending events (bending radius ≈4 mm) with decent device performance (EQE ≈ 2.6% at a brightness of 1000 cd m^{-2}).[75]

4.3. Advanced Patterning Methods and Key Challenges for Flexible PeLEDs

Most of the reported PeLEDs rely on spin-coated emitting layers. Alternative and more effective fabrication methods are crucial for development of highly pixelated, flexible PeLEDs. Vapor deposition methods yield high quality perovskite absorbing layers in photovoltaic devices with ≈20% power conversion efficiencies.[76] Compared to spin-coating and other solution-based techniques, these methods offer small batch-to-batch variation and they circumvent the complications arising from solvents (solvent compatibility, solvation-related impurity phases).[77] As

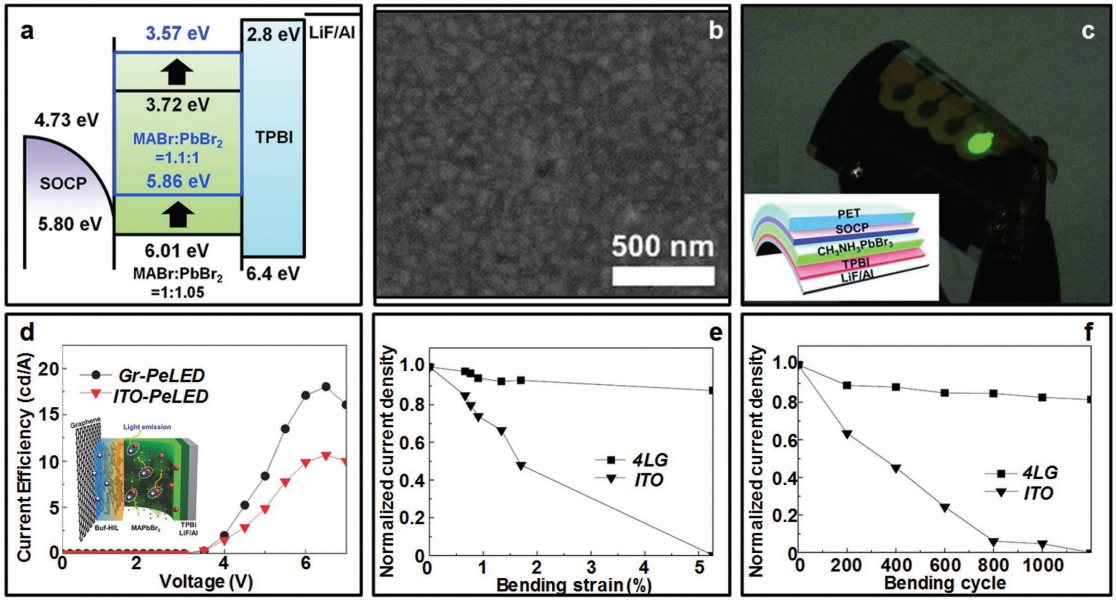

Figure 12. a) Energy band diagram of PeLEDs with $MAPbBr_3$ as the emitting layer, showing a decrease in ionization energy with increasing MABr molar proportion. b) SEM image of the $MAPbBr_3$ layer with an average grain size of ≈100 nm. c) Photograph of a flexible PeLED on a PET substrate with device structure shown in the inset. Reproduced with permission.[70] Copyright 2015, The American Association of Advancement of Science. d) Current efficiency–voltage characteristics of PeLEDs with graphene or ITO as the anode. The inset shows a schematic illustration of the device structure and efficient light emission in graphene-PeLEDs. e,f) Normalized current density of flexible graphene- and ITO-PeLEDs on PET substrate according to e) bending strains and f) bending cycles (strain: 1.34%, bending radius: ≈7.5 mm). Reproduced with permission.[72] Copyright 2017, Wiley-VCH.

summarized in a recent review,[77] these vapor-based methods, including coevaporation from dual targets (e.g., methylammonium iodide and $PbCl_2$[76a]), sequential vapor deposition, flash evaporation, and chemical vapor deposition, are also applicable to PeLEDs. Despite the inferior device performance (e.g., <0.1% and 4.36% for chemical vapor deposited and vapor-assisted solution processed $MAPbBr_3$ PeLEDs,[78] respectively), these vapor-based techniques, with further optimization in deposition conditions and improvements in film stoichiometry and others, represent potential alternatives toward flexible PeLEDs.

Screen-printing represents a scalable technique for large scale, low cost production. Proof-of-concept devices that exploit $MAPbBr_3$ and poly(ethylene oxide) as the emitting layers and carbon nanotubes and silver nanowires as the anodes/cathodes, can be achieved entirely by screen-printing in a layer-by-layer fashion on rigid or flexible substrates.[79] In the absence of charge injection/transport layers, PeLEDs printed on ITO/glass substrates show EQEs of ≈1.1% at 20 000 cd m^{-2}. An intriguing observation is that the performance of devices processed in an ambient environment surpasses that of devices prepared

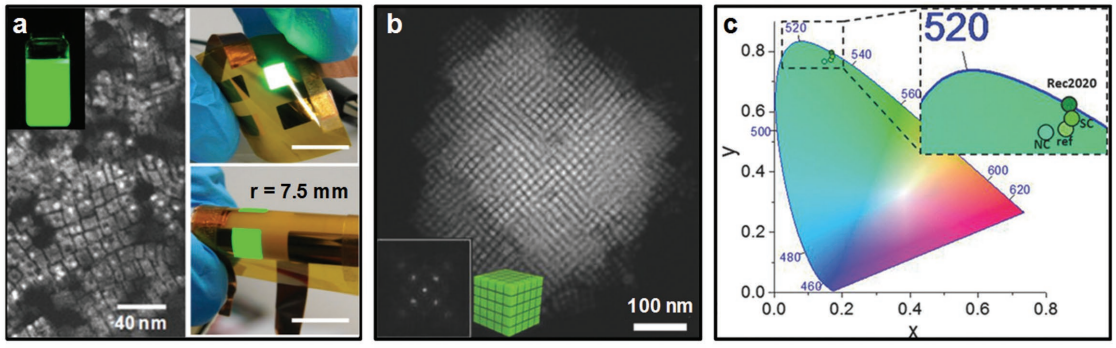

Figure 13. a) A flexible, ultrapure green PeLED using 2D $FAPbBr_3$ nanoplatelets as the emitting layer with color coordinates approaching the Rec. 2020 standard. (Left) TEM image of the 2D $FAPbBr_3$ nanoplatelets. Inset shows a photograph for a colloidal $FAPbBr_3$ dispersion that has a PL quantum yield of 88%. (Right) Photographs of a flexible perovskite LED at different bending radii (scale bars: 1 cm). Reproduced with permission.[73] Copyright 2017, American Chemical Society. b) Magnified high-angle annular dark-field STEM image of a single $CsPbB_3$ perovskite SC assembled from nanocubes (Inset: selected area FFT pattern of the supercrystal). c) CIE coordinates of the SC PeLED device (Inset: magnified view of the color coordinates of $CsPbBr_3$ SC, isolated nanocrystals of $CsPbBr_3$ (labeled "NC"), and 2D $FAPbBr_3$ nanoplatelets (shown in (a), labeled "ref") in comparison with the recommended pure green (Rec2020) color). Reproduced with permission.[74] Copyright 2018, Wiley-VCH.

in inert atmosphere. This result likely follows from humidity-induced enhancements in the PL due to partial solvation of methylammonium parts and self-healing of perovskite lattices. Fully printed PeLEDs on 200 μm thick polyacrylate substrates show a low turn-on voltage of 2.6 V and can undergo several cycles of bending to radii of ≈5 mm at 2% strain. Despite the inferior EQEs (0.14% when printed on flexible substrates), these screen-printing techniques are potentially amenable to low cost, roll-to-roll fabrication of arrays of PeLEDs on flexible substrates.

Patterning of perovskites with microscale precision represents a remaining challenge in integration of perovskite-based devices (LEDs, photodetectors, etc.) into advanced optoelectronic platforms. The instability of these materials in aqueous solutions and organic solvents prevents their patterning by conventional microfabrication procedures. A recently proposed strategy exploits a poly(methyl methacrylate) lift-off process and deep UV lithography to enable micropatterning of $MAPbI_3$ perovskites with high precision and in both lateral and vertical directions.[80] A key step uses chlorobenzene as the lift-off solvent, which dissolves poly(methyl methacrylate) without affecting the perovskites. Using this method, $MAPbI_3$ based transistors and photodetectors can be patterned on flexible substrates to yield devices with good electrical performance and high mechanical stability at bending radii of 6 mm. This patterning capability, though demonstrated for other types of devices, may also be applicable to flexible PeLED arrays with elaborate designs and their incorporation in integrated, flexible optoelectronic systems.

Compared to flexible OLEDs or QLEDs, flexible PeLEDs are still in early stages of development. Despite their impressive color purity, several key hurdles remain. From the electrical viewpoint, it is interesting to note that almost all examples of flexible PeLEDs are monochromic with green emission, likely due to well-established synthetic protocols and device layouts for $PbBr_2$-based perovskites. Efficient and balanced emission in red, green, and blue colors must be achieved for PeLED devices with full-color and white emission. In addition, long term device stability in the presence of a combination of air, moisture, light, and heat remains as a major issue for all types of devices based on metal halide perovskites. Moisture is particularly detrimental to the long term integrity of perovskites, which are highly ionic and thereby intrinsically unstable in hydrophilic environments.[7c] The decomposition of $MAPbI_3$ and other perovskites also involves oxidation processes presumably induced by the diffusion of photogenerated superoxide anions on halide vacancies.[64a] Chemical designs of perovskites with hydrophobic, long-chain organic cations can lower the sensitivity to moisture and encapsulation methods can enable minimal air and water permeability, as means to improve the stability of PeLEDs.[67a] In terms of mechanical properties, current flexible PeLEDs are bendable but not stretchable or deformable in other mechanical modes. Adapting fabrication concepts and mechanical designs from flexible QLEDs may be useful in this context. Finally, as with QLEDs, toxic elements such as Pb in perovskites place stringent limitations on their use in consumer electronics, especially those located at biointerfaces. Addressing this safety and environmental concern demands the developments of efficient Pb-free perovskite emitters.

5. Flexible 2D Materials-Based LEDs

2D materials are atomically thin layers with strong intraplane covalent bonding and weak interplane van der Waals interactions.[12b] Such materials can support a wide range of electrical behaviors, ranging from conductors (graphene), direct bandgap semiconductors (e.g., transition metal dichalcogenides (TMDs) and black phosphorus), and insulators (hexagonal boron nitride (hBN)).[81] The universal van der Waals interactions present in all 2D materials enable stacking of layers with highly dissimilar chemical and physical properties (compositions, band structures, lattice parameters, etc.), leading to heterostructures with unprecedented properties and functions in devices.[82] From the mechanical perspective, atomically thin 2D materials are intrinsically flexible by virtue of bending strains that decrease linearly with thickness.[12b] Moreover, the elastic strain limits of 2D materials compare favorably with those of conventional, state-of-the-art semiconductors.[12b] For example, TMDs show significantly higher elastic strain limits (by a factor of 4 or more) than III–V semiconductors (**Figure 14**a), mainly due to the much higher strength of covalent compared to ionic bonds. These electrical and mechanical attributes make 2D materials attractive candidates in flexible optoelectronic devices.[81,83] More specifically, graphene and TMDs can be deployed as important components (e.g., electrode or charge transport layers) in flexible LEDs.[7d,83a,84] This section focuses on recently developed flexible ILEDs with 2D materials as emitting layers, mainly enabled by materials chemistries and heterostructure designs.

5.1. Flexible LEDs Based on TMDs

TMDs with the formula of MCh_2, where M is a transition metal (typically Mo or W) and Ch are (mixed) chalcogens, represent an important class of 2D emitters. Monolayers of TMDs are direct bandgap semiconductors with emission wavelengths readily tunable in the visible spectrum via compositional control (Figure 14b).[82,85] Simple chemical treatment with an organic super acid passivates the surface defects and yields single layered TMDs with near unity PL efficiencies (Figure 14c).[86,87] Despite the high PL efficiency, LEDs based on TMDs emitting layers suffer from large charge injection barriers due to the Schottky contacts. Consequently, electroluminescence occurs only in limited areas around the metal contacts.[85,88] To overcome these problems, heterostructure designs (p–n junction formation[89]) and electrical operation modes (AC pulse[85]) can be explored to enable large area, steady-state electroluminescence. Among these, the use of van der Waals heterostructures with carefully designed sequences of atomically thin layers underpins to some of the most important progress in 2D materials-based LEDs. The most enabling feature for these heterostructures is the versatile band structure engineering that follows from the use of 2D materials of different compositions and numbers/thicknesses of layers.[90] The first van der Waals heterostructured LEDs involved graphene for the electrodes, hBN as the tunneling barriers, and TMDs quantum wells (MoS_2 or WSe_2) as the emitting layers, all assembled in a layer-by-layer fashion (**Figure 15**a).[90a] Under proper bias, the

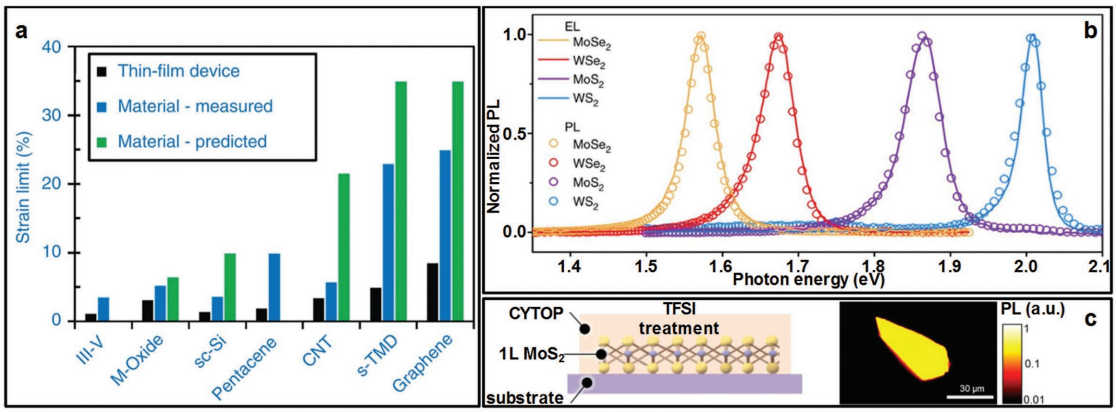

Figure 14. a) Comparison of maximum elastic strain limits of 2D materials with other conventional bulk semiconductor materials. Reproduced with permission.[12b] Copyright 2014, Nature Publishing Group. b) Electroluminescence (lines) and PL (circles) spectra of various transition metal dichalcogenide monolayer devices. Reproduced under the terms of the CC BY 4.0 license.[85] Copyright 2016, The Authors, published by Nature Publishing Group. c) (Left) Schematic illustration of a monolayer of MoS_2 coated by CYTOP and subsequently treated by bis(trifluoromethane)sulfonamide (TFSI). (Right) PL image of a MoS_2 monolayer after CYTOP coating and TFSI treatment, showing a near unity PLQY. Reproduced with permission.[86] Copyright 2017, American Chemical Society.

Fermi levels of graphene bottom and top electrodes move across the bottom of the conduction band and the top of the valence band of TMDs, respectively, allowing efficient charge carrier injection and recombination. LEDs with multiple (3–4) quantum wells stacked in series show EQEs up to 8.4% at low temperatures.[90a] Quantum wells composed of two different TMDs (MoS_2 and WSe_2) enable fine-tuning of the emission spectra while maintaining high EQEs (≈2% at room temperature, as shown in Figure 15b). These values represent record efficiencies for 2D materials-based LEDs. The intrinsic, ultrathin nature (10–40 atoms-thick) of van der Waals structures seamlessly align with core concepts in flexible optoelectronics. 2D LEDs stacked on PET substrates show unchanged device performance when bent to uniaxial strains up to 1% (Figure 15c).

5.2. Flexible LEDs Based on Graphene Derivatives

Another demonstration of flexible, 2D materials-based light emitting devices exploits the gate voltage dependent electroluminescence of graphene derivatives in transistor configurations.[91] Pristine graphene composed of one or few layers of covalently bonded carbon atoms is an ideal conductor with zero bandgap. Modifications of graphene with other atoms and functional groups offer versatile control over its optical and electrical properties and yield graphene-based derivatives with tunable bandgap structures. In a transistor-type device with reduced graphene oxide (rGO) as the gate, source and drain components, and graphene oxide (GO) as the dielectrics, a stack of semi-reduced GO semiconducting layers shows electroluminescence under applied bias (**Figure 16**a,b). The electroluminescence mechanism can be explained by the Poole–Frenkel process in which the injected electrons are excited to the lowest energy level of conduction band followed by radiative recombination with holes in π-bands. As the gate voltages increase, the level of the lowest unoccupied energy moves up and shifts the emission wavelengths from red (750 nm) to blue (450 nm) (Figure 16c). Flexible, all-graphene-based devices on bent PET substrates (bending radius of ≈8 mm) preserve their emission properties (Figure 16b). This type of gate-modulated, tunable emission may be attractive for certain applications. Single-layer or few-layer graphene with sizes of several nanometers (also known as graphene quantum dots (GQDs)) also shows tunable emission in the near UV and visible range.[92] The emission mechanism of GQDs, however, is complex and could stem from a combination of quantum confinement, edge effects, and others.[92b] A plausible mechanism, based on recent theoretical and experimental studies,[93] classifies the emission into intrinsic (from aromatic sp^2 carbon hexagons) and extrinsic states (from defects such as oxygen-containing groups). High quality GQDs synthesized by intercalating graphite with potassium–sodium tartrate show low oxidation states or defects and thus emit in the near UV range (centered at ≈400 nm) primarily due to the intrinsic electroluminescent mechanism.[92b] LEDs employing these GQDs as emitting layers achieve luminance over 1000 cd m^{-2} at 16 V and luminous efficiency of 0.65 cd A^{-1} at 1 mA cm^{-2}, which are among the highest reported values in GQD-based LEDs. The low cost and high biocompatibility make GQDs potential candidates in flexible ILEDs.

Despite the promising electrical and mechanical properties, LED devices that use 2D emitting materials, on rigid or flexible substrates, are far inferior in performance and cannot rival other types of flexible ILEDs. Key breakthroughs in the designs of materials and device structures are necessary. Another challenge for 2D based (flexible) LEDs is their complex growth and fabrication processes. Construction of van der Waals heterostructures of 2D materials typically requires mechanical exfoliation and consecutive stacking of individual layers. Existing methods for these purposes are not amenable to scalable fabrication of devices with elaborate structural designs. Emerging fabrication methods exploit ink-jet printing techniques and water-based, biocompatible ink formulations to

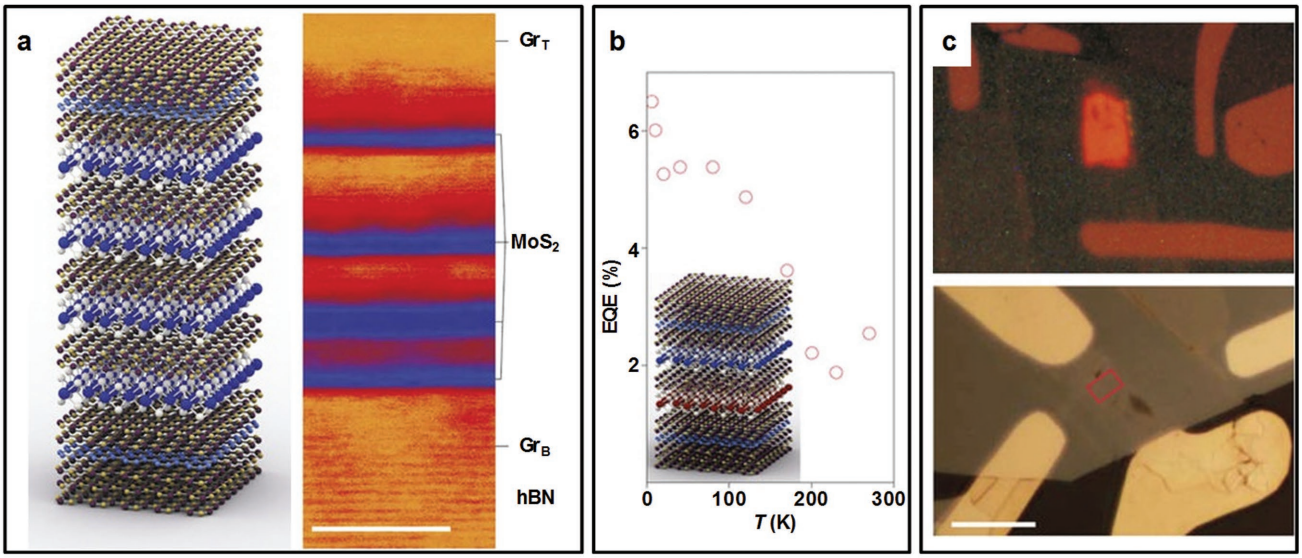

Figure 15. a) Schematic illustration and scanning transmission electron microscopy (STEM) image of the multi quantum well for heterostructure hBN/Gr_B/2hBN/MoS_2/2hBN/MoS_2/2hBN/MoS_2/2hBN/MoS_2/2hBN/Gr_T/hBN). The number of hBN layers between MoS_2 quantum wells in (a) varies. Scale bar, 5 nm. b) Temperature dependence of EQE for a device with two quantum wells made from MoS_2 and WSe_2. Inset: Schematic representation of a device with two quantum wells produced from different materials. c) Optical images of (Top) electroluminescence from a single quantum well device (hBN/Gr_B/3hBN/MoS_2/3hBN/Gr_T/hBN). $V_b = 2.5$ V, $T = 300$ K and (Bottom) a flexible, single quantum well device on PET collected in reflection mode. Scale bar: 10 µm. Reproduced with permission.[90a] Copyright 2015, Nature Publishing Group.

yield multistacked heterostructures of graphene, TMDs, and hBN in a high-speed fashion.[94] Photodetector arrays printed in this manner exhibit responsivities >1 mA W^{-1}, which compare favorably to values for devices made with mechanically exfoliated 2D materials. Similar printing techniques and ink formulation could potentially be applied to flexible 2D materials-based LEDs in a scalable manner.

6. Representative Applications of Flexible ILEDs in Displays, Wearable Electronics, and Implantable Biomedical Tools

The preceding sections highlight recent advances in flexible ILEDs from the materials perspective, with demonstrations at the device and systems levels. Flexible µ-ILEDs and QLEDs

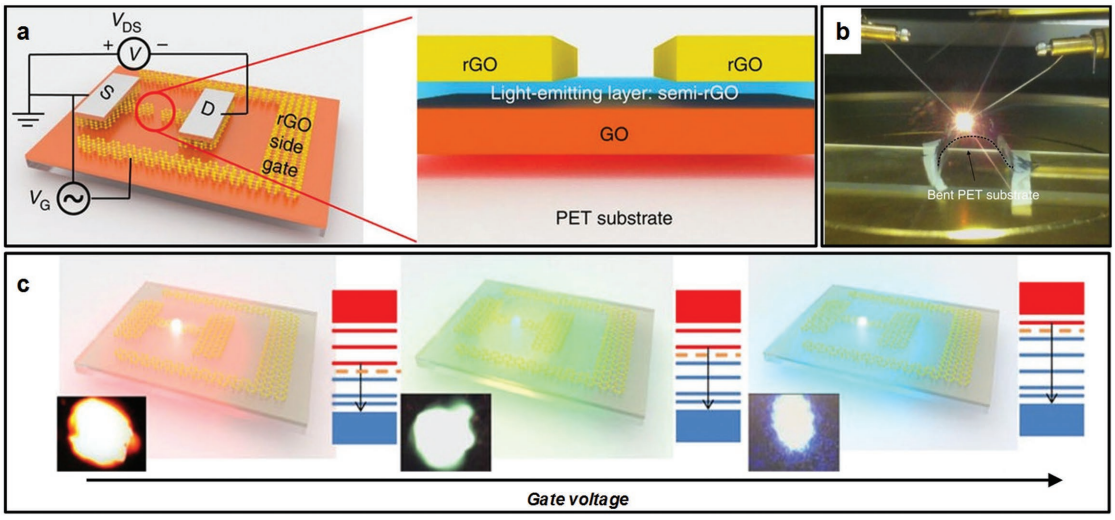

Figure 16. a) Schematic illustration of a graphene-based flexible LED. A distinct semi-reduced GO (blue) at the interface between GO (orange) and rGO (gold) is responsible for light emission. b) Bright red light emission from the graphene-based LED on a flexible PET substrate under a 12 V bias voltage and a 0.1 A drive current. The size of the device is around 100 µm × 100 µm. The bending radius is about 8 mm. c) Schematic illustration of the gate voltage-dependent electroluminescence. The Fermi level (orange dashed lines) determines the lowest unoccupied energy state that mainly participates in the radiative recombination. Inset: corresponding emission images from a real device. Reproduced under the terms of the CC BY 4.0 license.[91] Copyright 2015, The Authors, published by Nature Publishing Group.

with attractive electrical properties and levels of mechanical flexibility have been incorporated in optoelectronic platforms for various existing and emerging applications, ranging from highly deformable, next-generation displays, to sensing and visualization modules in smart wearable electronics, and to miniaturized, implantable biomedical tools for neural modulation and clinical therapy.[1,13,49a,b,50,56,59,84a,95] The unique material properties, device characteristics, and the associated advantages/disadvantages lead to different targeted applications for these two classes of flexible ILEDs. This section summarizes some representative uses of μ-ILEDs and QLEDs, especially in biomedical tools that couple intimately to soft and curvilinear surfaces of biological tissues for sensing and modulation.

6.1. Representative Applications of Flexible μ-ILEDs

High-yield assembly techniques and established design strategies make interconnected collections of μ-ILEDs highly promising candidates for next-generation flexible displays. As shown in Section 2, monochromic (red and blue) displays that harness the wafer-level performance and reliability of μ-ILEDs show exceptional flexibility and robust operation under extreme deformations. Adding other optical components such as patterned phosphor tiles and thin-film optical diffusers to blue μ-ILED arrays yields flexible, white-emitting modules (**Figure 17**).[13f] The microscale dimensions (down to $3 \times 10\ \mu m^2$, as presented by Xceleprint[12c]) and sparse distributions of the μ-ILEDs allow for high luminance across large areas (over 100 times larger than those for commercial LED dies with the same total amount of active materials) with additional unused space for other optoelectronic components such as driver circuits, sensors, and other components. These small area coverages also enable display systems with high levels of transparency. Stacking multilayers of μ-ILED arrays with proper spatial offsets between layers can provide unique 3D effects and also options in populating the open spaces, for displays or solid-state lighting systems.[13c] The most recent, advanced implementation of μ-ILED pixels and printed microscale integrated circuits yields high-resolution displays in flexible or rigid formats, capable of scaling to large areas. **Figure 18** highlights small prototypes, consisting of 1.4 inch passively driven, flexible displays composed of 128 × 128 InGaN-based blue pixels (each with a dimension of 8 μm × 15 μm) with resolution of 127 p.p.i. The displays show no degradation in illuminance when flexed. Sequential transfer printing of blue and green InGaN μ-ILEDs and red AlInGaP μ-ILEDs in aligned patterns (320 × 160 RGB pixels with 360 μm pixel pitch) enables the realization of 5.1 inch, full-color displays with resolution of 70 p.p.i. **Figure 19** demonstrates some of these displays with vivid colors, showing images of various objects, scenes, and portraits, including some devices that integrate microscale silicon integrated circuits distributed across and directly on the panel substrate, for high speed, digital operation.

One of the most enabling features of μ-ILEDs is that they can laminate conformally onto soft and curvilinear surfaces without notable changes in device performance. This capability allows their system-level implementation in a series of emerging biomedical and surgical tools for physiological monitoring, optical/electrical modulation, and clinical therapy. All such applications require bioinert chemistries at biotic/abiotic interfaces and encapsulation materials that prevent biofluid penetration for chronic implantation.[13c,d] Choices of materials and strategies for robust encapsulation of devices against biofluids appear in recent reports and reviews.[97] A flexible μ-ILED array encapsulated by PDMS can be manipulated with a conventional needle and used as a light emitting suture in an animal model.[13c] PDMS, as biocompatible barriers to surrounding tissues and biofluids, render μ-ILEDs water-proof and are fully operational even when completely immersed in biofluids. Subdermal implantation of such "photonic" sutures could accelerate wound healing, provide in vivo illumination in deep tissues, and serve as transducers of important

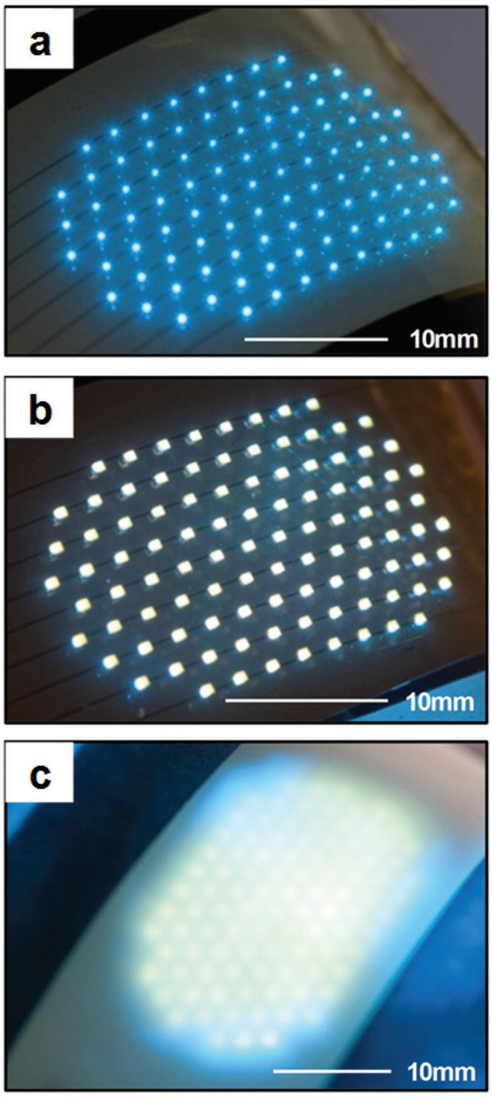

Figure 17. Optical images of a fully interconnected array of InGaN μ-ILEDs: a) blue-emitting without phosphor, b) with a laminated film of encapsulated YAG:Ce phosphor islands (500 μm × 500 μm), and c) with a laminated diffuser film to achieve diffuse, large area white emission. Reproduced with permission.[13f] Copyright 2011, The National Academy of Sciences.

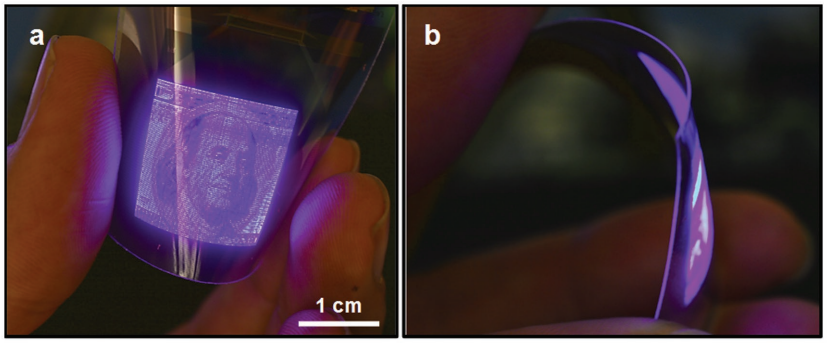

Figure 18. Photographs of 1.4 inch, passively driven flexible displays composed of 128 × 128 blue pixels (127 p.p.i.) patterned by transfer printing on 125 µm thick PEN substrates, showing the image of a US bill. The blue pixels are InGaN-based µ-ILEDs with sizes of $8 \times 15\ \mu m^2$ and pitch of 200 µm. Reproduced with permission.[96] Copyright 2017, Society for Information Display, published by John Wiley & Sons.

physiological parameters or vital signs. Functional systems that integrate µ-ILED arrays with photodiodes are capable of monitoring changes in surrounding bioenvironments. For example, a stretchable µ-ILED array integrated with molded plasmonic crystals laminates seamlessly on a tubing suitable for use in intravenous delivery systems (inset in **Figure 20**a). With an external photodetector, this system can detect changes in refractive-indices of fluids that pass through tubing. As these changes correlate well with the types and contents of fluids and relevant biomaterials (e.g., glucose as illustrated in Figure 20a), this system can be used in surgical tools of relevance for continuous monitoring of the nutrient dosage or clinical medicine.[13c] An advanced version of this photometry system involves cointegration of µ-ILEDs and microinorganic photodetectors (µ-IPDs) in stretchable formats. As an object approaches or moves away for the sensor, the change in the photoresponse of the µ-IPDs correlates to changes in relative distance. Figure 20b shows such an optical proximity sensor mounted on the fingertip of a glove and the dependence of the photocurrents on distance.[13c] The exceptional mechanical properties and robust operation of µ-ILEDs under extreme mechanical deformation allow their integration in surgical tools such as balloon-catheters that involve significant changes in shape during operation (e.g., in inflated and deflated states, as shown in Figure 20c). Balloon-catheters functionalized with heterogeneous collections of high-performance semiconductor µ-ILEDs, sensors, and actuators offer new capabilities to sense physiological signals and stimulate tissues during operation.[13d] µ-ILED arrays mounted on this type of multifunctional surgical tool enable programmable light delivery to targeted regions with high spatial precision.

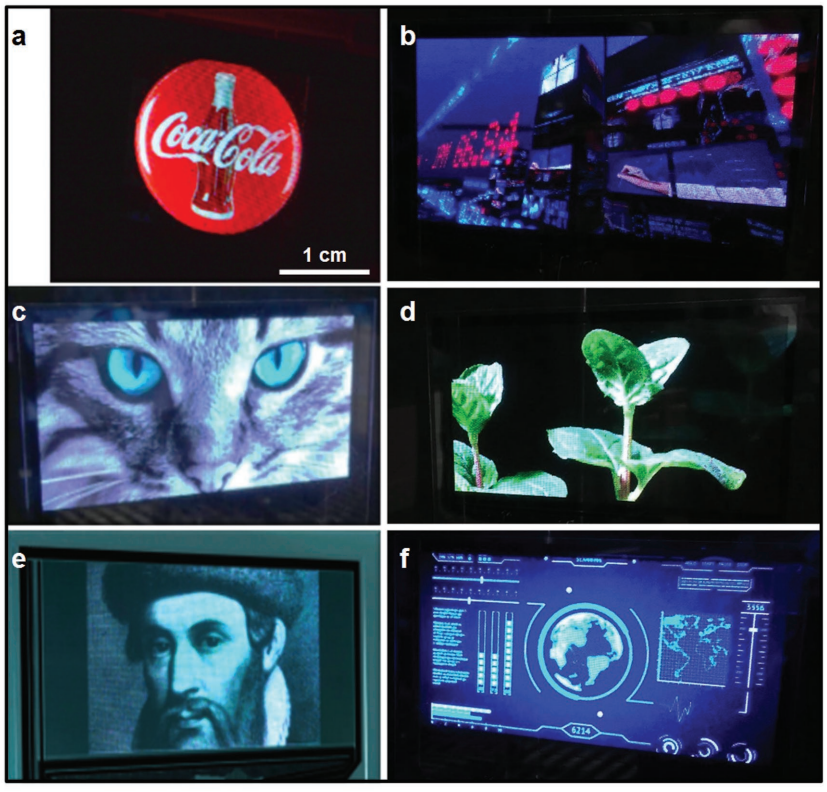

Figure 19. Photographs of full-color displays of µ-ILED RGB pixels patterned by transfer printing on 700 µm thick aluminosilicate substrates. a) A small area full-color display driven by passive matrix showing a Logo. Reproduced with permission.[96] Copyright 2017, Society for Information Display, published by John Wiley & Sons. b–f) 5.1 inch diagonal active matrix µ-ILED displays with 320 × 160 pixels (70 p.p.i.) showing various images, scenes, and portraits. The blue and green pixels are InGaN-based µ-ILEDs while the red ones are AlGaInP µ-ILEDs. The size of each µ-ILEDs is 8 × 15 µm and the pitch is 360 µm. Reproduced with permission. Copyright 2018, Xceleprint, Inc.

The capability of µ-ILEDs to deliver light into biological structures at the sites of interest also allows their use in an emerging field of neuroscience, known as optogenetics,[98] that utilizes light to selectively stimulate or inhibit neural activity in targeted cell types.[13j,k,27b,95,99] Together with genetic modification techniques, light-modulated neural activity can provide important clues into the connections between animal behavior and associated neural networks in the brain. Conventional light delivery methods in this context rely on optical fibers originally designed for telecommunications.[100] The resulting physical tether, however, constrains and restricts the natural behaviors of the animals, sometimes in a way that frustrates the interpretation of associated neuroscience experiments. Here, µ-ILEDs serve as the foundations for advanced optogenetic tools, in the form of thin, flexible filaments that are fully implantable with minimal invasiveness and wireless operation in freely moving animals.[13j,k] The physical sizes of "cellular scale" InGaN µ-ILEDs (6.45 µm thick and

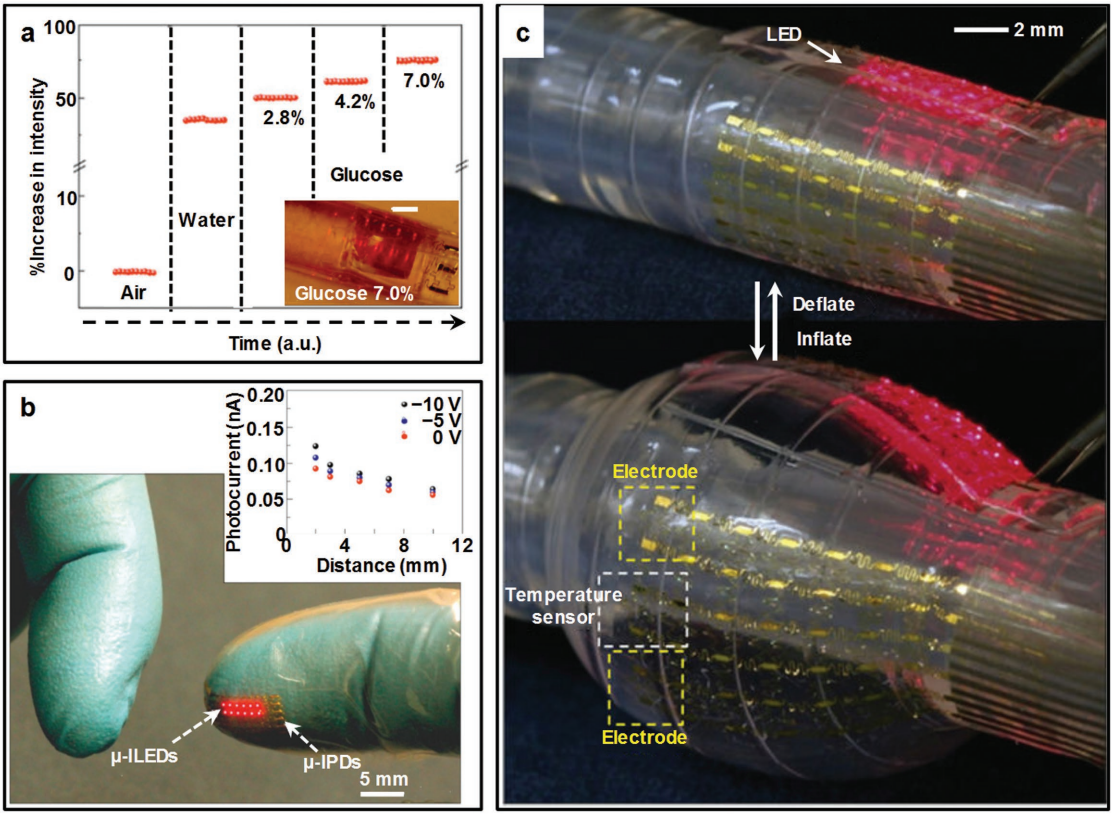

Figure 20. a) Measurement results from a representative refractive-index microsensor. (Inset) The sensor integrates an array of μ-ILEDs and molded plasmonic crystals, which laminates directly on a flexible plastic tube. The measurements correspond to a sequence of glucose solutions passed through the tube. Scale bar = 1 mm in inset. b) Optical image of a proximity sensor with arrays of μ-ILEDs (4 × 6) and μ-IPDs, transfer printed on the fingertip region of a vinyl glove. The inset shows a plot of photocurrent as a function of distance between the sensor and an object (white filter paper) for different reverse biases and different voltages. Reproduced with permission.[12] Copyright 2010, Nature Publishing Group. c) Optical image of a multifunctional balloon-catheter in deflated and inflated states. The image shows arrays of temperature sensors (anterior), μ-ILEDs (posterior), and tactile sensors (facing downward). Reproduced with permission.[13c] Copyright 2011, Nature Publishing Group.

50 μm × 50 μm in area) and mechanical properties of the complete injectable platforms minimize tissue damage, with lesions that are much smaller than those of optical fibers.[13j] The high efficiency in operation and designs that facilitate thermal transport, together with the natural convective cooling provided by flow of blood and cerebrospinal fluids, allow μ-ILEDs to serve as implantable optogenetic stimulators with minimal changes in temperature (≈0.1 °C at an output power of 10 mW mm^{-2}) or adverse effects on the surrounding fragile neural tissues.[99b,f,101] The resulting platforms after encapsulation are also biocompatible for chronic, stable operation within the demanding set of conditions associated with bioenvironments.[99a,102]

In addition to these attractive mechanical, thermal, optical, and biocompatible characteristics, injectable platforms that use μ-ILEDs as light sources offer unique advantages compared to existing fiber-based systems. i) Both unidirectional and bidirectional illumination patterns can be realized with μ-ILEDs.[13j] Such illumination profiles are advantageous for stimulating certain brain regions in small animal models, such as the oblong shaped basolateral amygdala in rodents.[99c] In addition, a single injectable, miniaturized filament/platform consisting of arrays of flexible μ-ILEDs of the same or different colors provides multichannel operation capabilities in independent control of multiple neuronal subpopulations and supports spatiotemporal modulation and functional mapping of multisites in brains.[27b,99e] For instance, an implantable array of red-emitting μ-ILEDs settled on the meningeal space between the skull and brain surface can modulate motor neurons of specific regions in mouse brain with promise in high-resolution, detailed mapping of motor cortical areas for various body movements.[27b] ii) Transfer printing allows for integration of multiple functional layers with capabilities in temperature sensing, optogenetic stimulation, photometric measurements, and electrical recording, all in a single injectable platform with dimensions smaller than those of conventional unimodal optical fibers (**Figure 21**).[13j] Another multimodal platform combines the capabilities of optogenetic simulation enabled by InGaN μ-ILEDs with drug delivery via soft microfluidic channels (**Figure 22**a,b). Here, thermally and wirelessly activated pumps deliver up to four different drugs with μL-scale precision from separate channels.[13k] These features enable programmable, independent optogenetic and pharmaceutical controls over behaviors of animal models without the brain trauma associated with implanted cannulas (Figure 22c). iii) μ-ILEDs can be integrated with compact wireless systems for power and control. The most advanced power modules (metal coils with

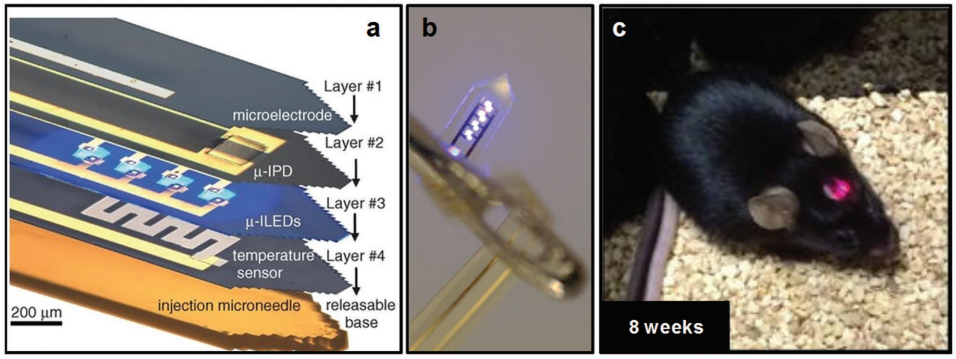

Figure 21. a) A multifunctional, implantable optoelectronic device, in a tilted exploded view layout illustrating various components: electrophysiological measurement (no. 1: Pt contact pad, microelectrode), optical measurement (no. 2: silicon μ-IPD), optical stimulation (no. 3: GaN μ-ILED array), and temperature sensing (no. 4: serpentine Pt resistor), all bonded to a releasable structural support for injection (microneedle). b) A photograph of a wirelessly powered, flexible integrated system, highlighting the four blue-emitting μ-ILEDs at the tip. Reproduced with permission. Copyright 2013, The American Association for Advancement of Science.[13j] c) A healthy, freely moving mouse (8 weeks after the device implantation) with lightweight, flexible wireless systems powering GaN μ-ILED arrays in the ventral tegmental area of the brain. Reproduced with permission.[99f] Copyright 2017, Elsevier.

9.8 mm in diameter and maximum thickness of 1.3 mm)[99f] rely on resonant magnetic coupling energy transfer schemes and are easily adaptable to a variety of enclosures used to study animal behavior. The result is a broad collection of injectable optogenetic platforms with tether-free operation, on freely moving animals (Figure 21c) capable of use in conventional scenarios as well as those (e.g., social experiments) where conventional fiber or head-mounted systems would result in parasitic, confounding challenges.[13j,k] Besides powering schemes that use resonant inductive coupling, recent work highlights a "self-powered," ultracompact (typical size ≈220 μm × 220 μm) light source that integrates photovoltaic diode layers and LED layers, monolithically in the same device stack (9 μm thick).[103] Here, the photovoltaic unit captures external, low-energy IR photons (≈810 nm) and provides photogenerated currents and voltages capable of driving LEDs with higher-energy, visible emission (630 or 590 nm), thus enabling IR-to-visible upconversion in an engineered material structure with a practical quantum yield over 1%. Under external IR excitation, such implantable, miniaturized light sources demonstrate the capabilities in wireless optogenetic control of in vitro and in vivo neural activities.

6.2. Representative Applications of Flexible QLEDs

The extended color gamut, facile solution processability, and emerging patterning techniques make QLEDs promising candidates in low cost, high-resolution flexible displays that can rival state-of-the-art OLED-based systems. Following efforts on both materials and mechanical aspects, the electrical performance

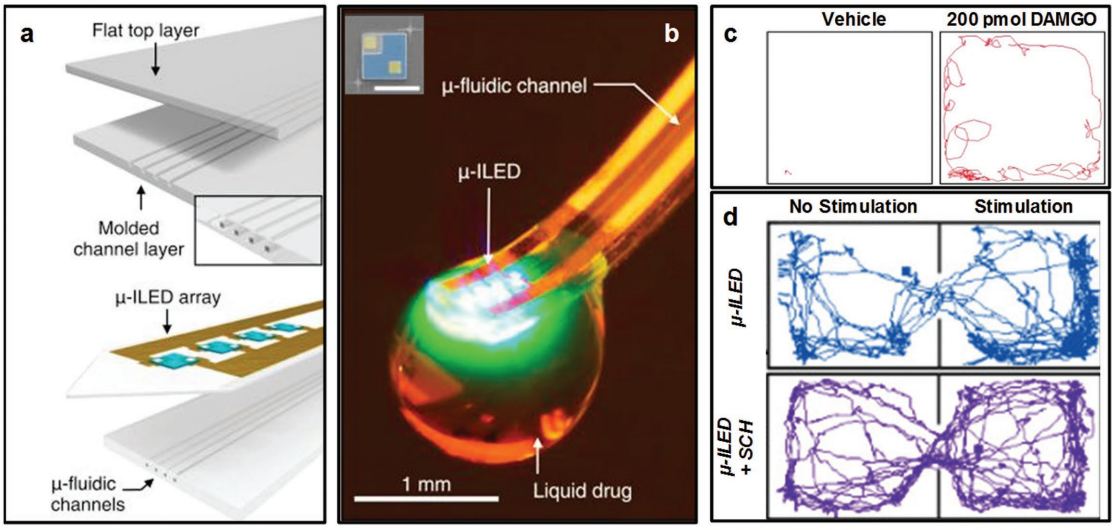

Figure 22. a) Schematic diagram of the integration of a soft, four-channel microfluidic probe with a flexible array of blue-emitting μ-ILEDs (each with lateral dimensions of 100 × 100 μm^2 and thicknesses of 6.54 μm) and metal interconnect traces on a film of PET (thickness of 6 μm). b) Optofluidic neural probe during simultaneous drug delivery and photostimulation. Inset shows a colorized SEM image of a μ-ILED (scale bar: 100 μm). c) Representative traces of movement from the same animal for 2 min after drug delivery clearly show an increase in overall movement and rotations. d) Representative traces of movement during the real-time place testing experiment of one TH-Cre$^{VTA:ChR2}$ animal show a SCH23390-sensitive preference for the photostimulation-paired chamber. Reproduced with permission.[13k] Copyright 2015, Elsevier.

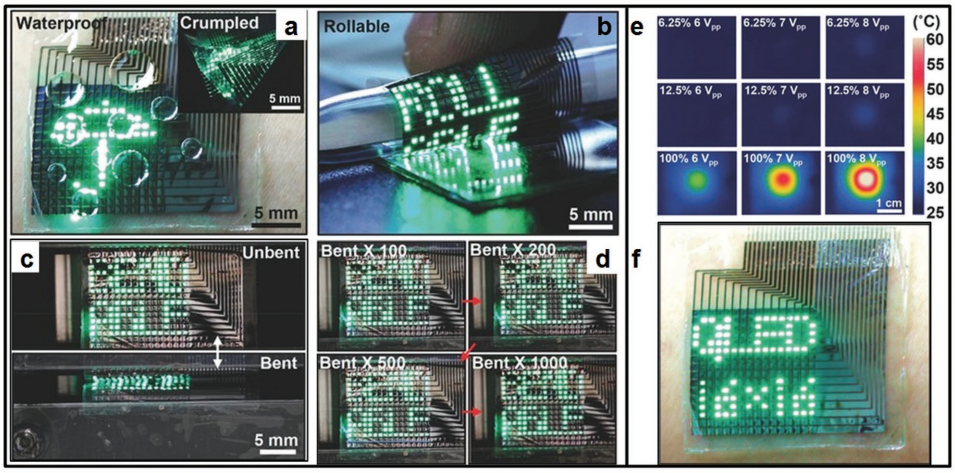

Figure 23. a–d) Photographs of stable operation of ultrathin QLED displays with a) water-proof property and in crumpled (inset in (a)), b) rolled, and c,d) bent states. e) Temperature rises of the QLEDs operated with different voltages and duty cycles. f) Photograph of a working QLED display mounted on the skin. Reproduced with permission.[56c] Copyright 2017, Wiley-VCH.

of flexible QLEDs now approaches industry standards[5,7b] (brightness 100–1000 cd m^{-2} and 1000–10 000 cd m^{-2} for displays and solid state lighting applications, respectively; lifetime over 10 000 h at 100 cd m^{-2}) with highest reported values of brightness over 40000 cd m^{-2}[56c] and lifetime over 10 000 h at 100 cd m^{-2}.[49b] Besides the potential use in ultrahigh-definition 4K and 8K TVs or other large area displays, one application of particular interest is the wearable QLED displays that involve conformal contact with human skin (**Figure 23**). The ultrathin form factor of QLEDs and the approach of placing fragile components near the NMP ensure their stable operation under bending, stretching, and other harsh distortional conditions such as crumpling and rolling, that exceed the deformation limits of skin.[49b,56c] Encapsulation layers composed of parylene and epoxy provide effective protection of wearable devices against water droplets and humidity conditions (Figure 23a). Well-encapsulated devices remain operational after 24 h soaking in water.[56c] Equally important for wearable applications, temperature increases of passively driven QLED arrays at low duty cycles (e.g., 16 × 16 arrays at 6–8 V peak-to-peak voltages with a duty cycle of 6.25%) remain below 28.5 °C (Figure 23e), with no adverse thermal effects on adjacent tissues. This operational mode involves low power consumption (0.144 W) while providing adequate brightness (674 cd m^{-2} at 6 V, for reference, maximum brightness of iPhone 7 is 625 cd m^{-2}).[56c]

The mechanical flexibility, water-proof operation, and thermal control allow the integration of QLED display modules and other electronic components into wearable platforms to monitor vital signs, physiological parameters, and properties of the surrounding environments (via sensors) and to display the results in real-time (via QLEDs). One example includes MoS_2 based resistive random-access memory (RRAM) devices, pressure sensors, and QLED arrays (**Figure 24**a).[59] Mechanical changes measured by pressure sensors are stored in memory devices for subsequent display via QLEDs. Another platform combines temperature sensors and accelerometers with QLED displays (Figure 24b).[56c] When worn on the wrist, this system can display information on temperature changes and step counts in real time. A touch sensor functions as the switch through which the user can toggle between two modes (temperature monitor and pedometer). Some emerging technologies, including augmented reality devices, smart surgical glasses, and smart windows, require "invisible" LEDs that do not affect the original appearance or functionality of the complete platform. QLEDs with transparent ITO anodes and cathodes can offer both high brightness (43 000 and 30 000 cd m^{-2} from the bottom and top, respectively, at 9 V) operation and high optical transmittance (90% at 550 nm and 84% over the entire visible spectrum), to yield high-performance transparent displays.[56a] Adapted from the previously discussed device architectures and mechanical designs, QLEDs with total thicknesses of 2.7 µm in wavy geometries exhibit extremely high bendability (radii of curvatures ranging from a few micrometers to hundreds of micrometers) and stretchability, for seamless integration on objects with various curvatures. In addition, transfer printing of assemblies of aligned RGB pixels yields full-color QLEDs in flexible and transparent formats, of particular interest for systems for augmented reality, internet of things, and wearable devices. Other than serving as the basis of visualization modules, flexible red-emitting QLEDs can also provide light sources in wearable optical sensors for photoplethysmography (PPG).[53] Transfer printing multilayer QLED stacks (Al/TiO_2/QD/TFB/graphene/PEN) in a single step to a prestrained PDMS substrate, followed by a buckling process, results in highly stretchable arrays of QLEDs. These devices can be stretched up to 70% strain without changes in optoelectronic performance. Similar fabrication procedures can be applied to PbS QD-based stretchable photodetector arrays. A wearable device that integrates stretchable QLEDs and photodetectors couples conformally with the skin (e.g., wrapped around a fingertip) and provides noninvasive, in situ monitoring of PPG (Figure 24c).[53]

In a broader context, light-responsive QLEDs represent an important, recent advance in this field.[43b] Realization of both efficient photocurrent generation and high electroluminescence within a single system stems from the unique band diagrams in heterogeneous DHNRs. The coexistence of type-I (between

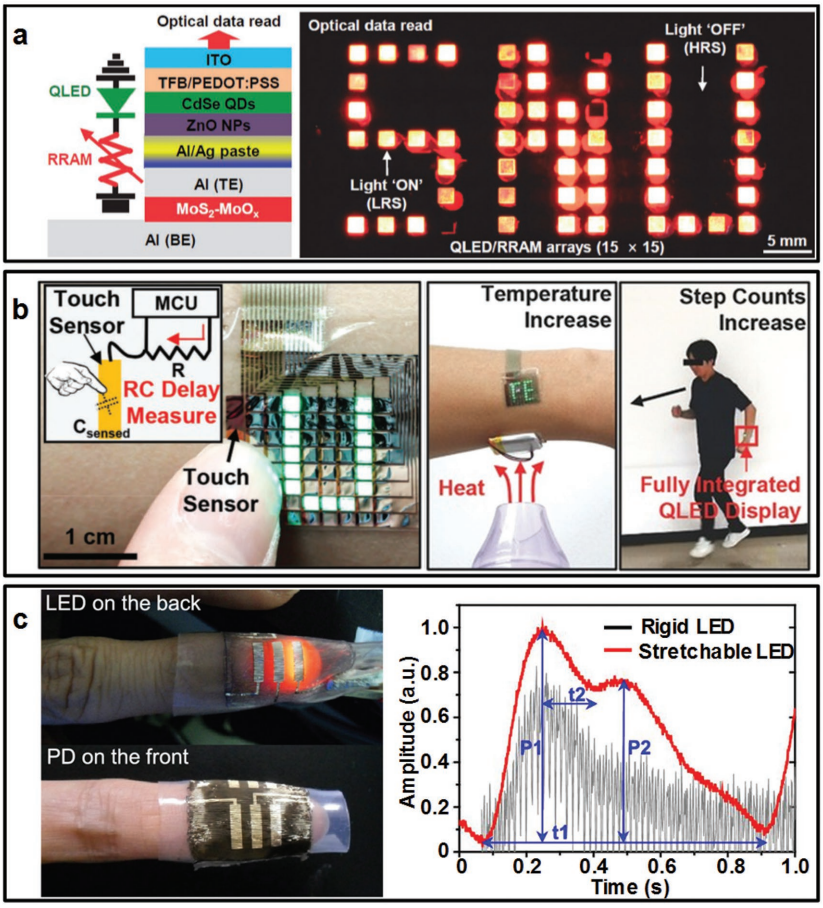

Figure 24. a) (Left) Schematic structure of an integrated system of MoS_2 RRAM and QLEDs. (Right) A photograph showing the optical reading through the 15 × 15 QLED array. Reproduced with permission.[59] Copyright 2016, Wiley-VCH. b) Photographs of (Left) the touch sensor integrated with the ultrathin QLED display and (Middle) the integrated wearable system subjected to external heat and (Right) a subject wearing the device while running. Reproduced with permission.[56c] Copyright 2017, Wiley-VCH. c) (Left) Skin-mounted PPG sensor composed of QLEDs during LED operation at 8.4 V and QD photodetectors wrapped around the finger of a subject. (Right) Real-time PPG signal pulse wave measured by a stretchable QD photodetector using the stretchable QLED or an ITO-based rigid QLED as a light source. Reproduced with permission.[53] Copyright 2017, American Chemical Society.

CdSe/CdS and CdSe/ZnSe) and type-II heterostructures (between CdS and ZnSe) (**Figure 25**a,b) enables switchablility between light-emitting and photodetection modes by applying forward or reverse bias. The dual-functional devices demonstrate high luminous efficiency (EQE of 8.0% at 1000 cd m^{-2} under 2.5 V bias) and high photoresponsivity (200 mA W^{-1}). These values compare favorably to state-of-the-art QLEDs and commercial silicon photodetectors. A straightforward demonstration of light-sensing capability of DHNR QLEDs involves a multilayered, 10 × 10 pixel device irradiated by a laser pointer (Figure 25c,d. A circuit board supplies forward bias to pixels under irradiation (i.e., turn on these LED pixels), which allows for demonstration of the "writing" action in response to laser irradiation. Figure 25e,f shows the temporal response of such devices in two different operational modes. The fast response in both electroluminescence and photocurrent generation modes (sub-microseconds to a few microseconds) empowers LED displays with the ability to respond to changes in light from the surroundings, as exemplified by displays with automatic brightness control and touchless user interface (Figure 25f), as well as direct display-to-display data communication systems. Though the reported DHNR-LEDs are fabricated on conventional rigid substrates, the same design concepts are readily applicable to flexible light-responsive LEDs.

7. Conclusion

Results summarized in this review highlight the rapid growth of the field of flexible ILEDs. Recent advances in materials designs, fabrication concepts, and assembly techniques underpin the emergence of high-performance, highly deformable ILEDs as well as their system-level integration into platforms with practical utility. These advanced optoelectronic platforms, such as next-generation displays and wearable/implantable biomedical tools, offer significant opportunities in applications that cannot be realized using existing technologies. Flexible μ-ILEDs fabricated from state-of-the-art III–V epitaxial layers and assembled by automated transfer printing techniques represent attractive choices for many of these applications, especially those related to biointegrated systems. The high brightness and efficiency, the mechanically compliant structures, and the long-term stable operation that is possible with biocompatible encapsulation layers allow for multifunctional, implantable tools for light delivery to broad classes of biological tissues. Of particular interest are injectable filaments with flexible μ-ILEDs for selective stimulation or inhibition of genetically targeted neuron groups in the brain and peripheral nervous system. Related classes of miniaturized implants with both light sources and light-sensing elements at target sites of interest facilitate multimodal dissection of neuronal circuits and enable new paradigms in neuroscience research.[99f]

These and other classes of ILEDs also enable low cost fabrication of flexible, ultrahigh resolution, full-color LED displays, and high color-purity lighting sources in large-area or portable/wearable formats. System-level integrated wearable platforms using QLEDs as displays or light sources represent an appealing type of bioelectronic devices that provide real-time measurements and visualization of physiological parameters and biomedical information of relevance. Compared to conventional III–V emitters, these new classes of materials feature remarkably tunable optoelectronic properties via versatile compositional control and structural engineering, which opens up unusual possibilities such as dual functional light sensitive LEDs.[43b] In addition to relatively well-studied QLEDs, other

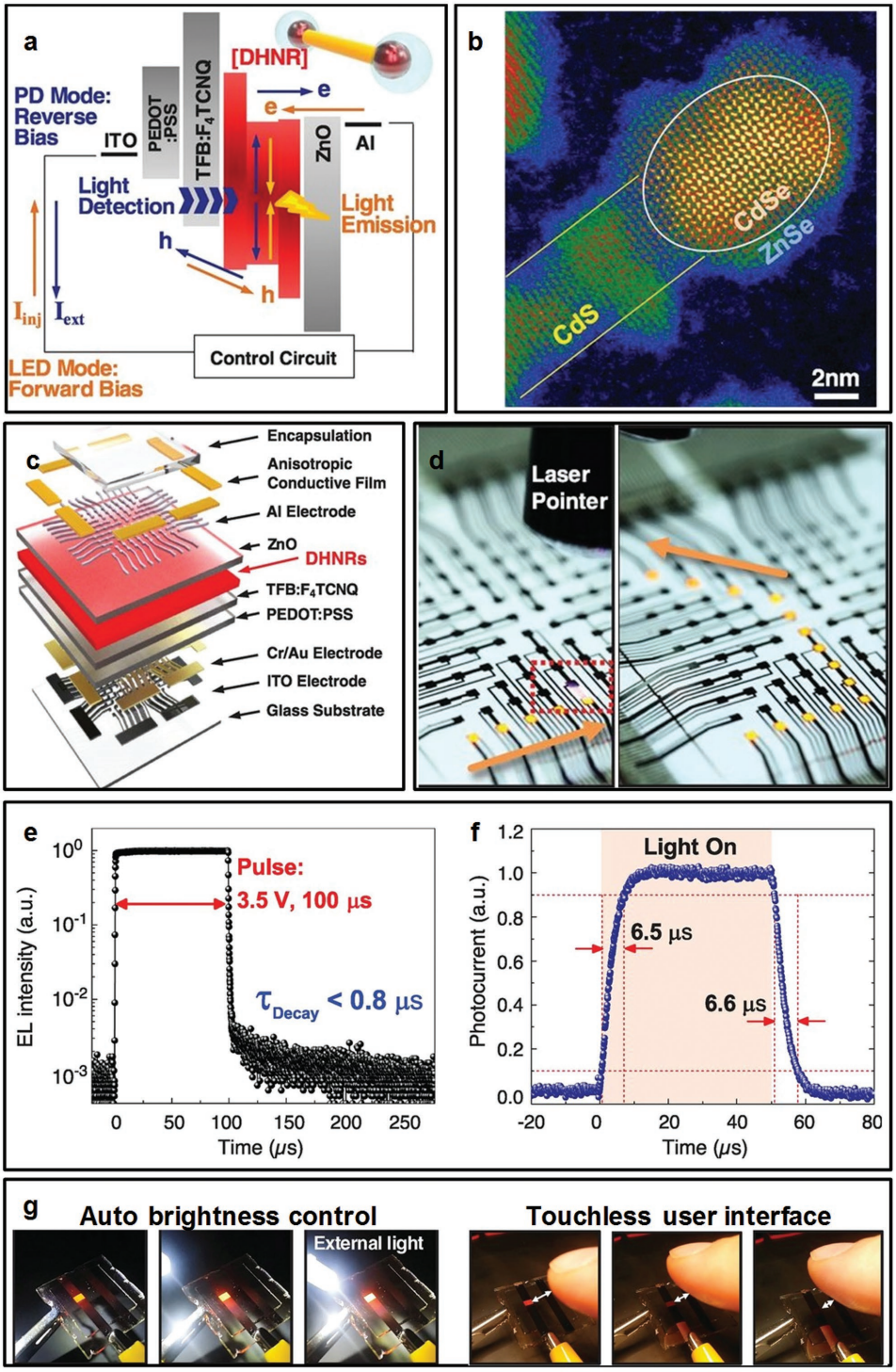

Figure 25. a) Energy band diagram of DHNR-LED along with directions of charge flow for light emissive (orange) and detection (blue) and a schematic of a DHNR. b) A high magnification STEM image of DHNRs. c,d) Schematic illustration and photograph of a 10 × 10 array of light-sensitive DHNR-LEDs. A laser pointer illuminates and turns on pixels along the path outlined by the orange arrows. e,f) Transient electroluminescence showing the decay time and photocurrent in response to illumination by a blue LED source driven by 3 V, 50 μs square-wave voltage pulses. g) Automatic brightness control at the single-pixel level in response to an approaching white LED bulb (Left) or a finger (Right) that blocks ambient light. Reproduced with permission.[43b] Copyright 2017, The American Association of Advancement of Science.

types of flexible ILEDs exploiting unconventional emitters also hold great potential in various emerging applications. Compared to QDs, perovskites show similar or even higher levels of control over color purity and tunability but require less stringent synthetic conditions and are thus readily available at lower costs. Although the device performance is still inferior to their

QD counterparts, flexible PeLEDs can be attractive for highly deformable displays and ultrapure photonic sources. LEDs based on 2D materials are still in early stages of development, with low EQEs. The atomically thin form factors of 2D materials align well with the core concepts in inorganic flexible electronics. Together with other 2D materials-based components, these flexible ILEDs may constitute advanced, multifunctional wearable platforms. On the other hand, many of these high-performance, emerging inorganic emitters, such as QDs or metal halide perovskites, contain toxic elements (e.g., cadmium or lead), which may limit their widespread use in consumer electronics, especially those involving chronic use as biomedical implants. The development of heavy-metal-free systems without compromised device performance continues to be an active topic for research in QDs and perovskites.[5] Success in these endeavors will greatly expedite the use of these flexible ILEDs in biointegrated systems.

The tremendous research progress in this field is beginning to yield impressive commercialized prototypes and actual products, especially in display systems. As mentioned above, Samsung has achieved 8K resolution TVs using QDs as down-converters for the backlight from blue LEDs. These and related products add momentum around the commercial development of self-emissive QLED displays, in flat or flexible formats. In parallel, start-up companies and major corporations have demonstrated high-definition, small and large area displays consisting of aligned μ-ILED RGB pixels. Xceleprint has achieved 5.1 inch, full-color μ-ILED displays (as illustrated in Figure 19), including systems that include printed microscale integrated circuits as drivers on the display substrate. Somewhat larger LEDs also serve as essential building blocks in large or even gigantic displays, such as the 146 inch "The Wall" from Samsung. Other major corporations, including Sony and Apple, are also developing TV and mobile displays based on microscale LEDs. Moreover, the established fabrication methods, device designs, and powering schemes for μ-ILEDs have also evolved into commercial products for biomedical and neuroscience applications. As a representative example, Neurolux has developed fully implantable, light weight, wireless tools with high-performance, ultraminiaturized μ-ILEDs, as well as software/hardware systems, for optogenetic studies in the brain and near spinal cords of freely moving animals.

Research efforts covered in this review encompass various types of materials as well as their applications at the device-, circuit-, and system-levels, and highlight the current state of this emerging field. Methodologies developed for one type of ILEDs can be applied to other types as well. For instance, the developments of stretchable QLEDs exploit many mechanical designs originally developed for μ-ILEDs. More generally, the toolbox of design concepts and processing principles developed for ILEDs can also be leveraged in other, related important components (photodetectors, transistors, lasers, etc.) for advanced optoelectronic platforms. Future opportunities for flexible ILEDs will follow from both fundamental and applied research efforts, especially that involve interdisciplinary studies, including materials chemistry of inorganic emitters, underlying physics of heterogeneous quantum structures, manufacturing science in microfabrication and scalable assembly techniques, optoelectronic device structure design, mechanical, and biochemical engineering, and biomedical and neurological science.

Acknowledgements

The authors acknowledge Xceleprint for providing images of the 5.1 inch μ-ILED displays fabricated by using micro transfer printing process. This review is part of the *Advanced Optical Materials* Hall of Fame article series, which recognizes the excellent contributions of leading researchers to the field of optical materials science.

Conflict of Interest

The authors declare no conflict of interest.

Keywords

bioelectronics, flexible optoelectronics, light emitting diodes, wearable devices

Received: July 18, 2018
Revised: August 17, 2018
Published online: September 20, 2018

[1] S.-I. Park, Y. Xiong, R.-H. Kim, P. Elvikis, M. Meitl, D.-H. Kim, J. Wu, J. Yoon, C.-J. Yu, Z. Liu, Y. Huang, K.-C. Hwang, P. Ferreira, X. Li, K. Choquette, J. A. Rogers, *Science* **2009**, *325*, 977.
[2] D.-H. Kim, N. Lu, R. Ma, Y.-S. Kim, R. H. Kim, S. Wang, J. Wu, S.-M. Won, H. Tao, A. Islam, K. J. Yu, T.-I. Kim, R. Chowdhury, M. Ying, L. Xu, M. Li, H.-J. Chung, H. Keum, M. McCormick, P. Liu, Y.-W. Zhang, F. G. Omenetto, Y. Huang, T. Coleman, J. A. Rogers, *Science* **2011**, *333*, 838.
[3] Y. M. Song, Y. Xie, V. Malyarchuk, J. Xiao, I. Jung, K.-J. Choi, Z. Liu, H. Park, C. Lu, R. H. Kim, R. Li, K. B. Crozier, Y. Huang, J. A. Rogers, *Nature* **2013**, *497*, 95.
[4] G. Gustafsson, Y. Cao, G. M. Treacy, F. Klavetter, A. Colaneri, A. J. Heeger, *Nature* **1992**, *357*, 477.
[5] J. M. Pietryga, Y.-S. Park, J. Lim, A. Fidler, W. K. Bae, S. Brovelli, V. I. Klimov, *Chem. Rev.* **2016**, *116*, 10513.
[6] S. Nakamura, G. Fasol, *The Blue Laser Diode: GaN Based Light Emitters and Lasers*, Springer-Verlag, Berlin/Heidelberg, Germany **1997**.
[7] a) B. R. Sutherland, E. H. Sargent, *Nat. Photonics* **2016**, *10*, 295; b) Y. Shirasaki, G. J. Supran, M. G. Bawendi, V. Bulovic, *Nat. Photonics* **2013**, *7*, 13; c) S. D. Stranks, H. J. Snaith, *Nat. Nanotechnol.* **2015**, *10*, 391; d) J. Shang, C. Cong, L. Wu, W. Huang, T. Yu, *Small Methods* **2018**, *2*, 1800019.
[8] D. A. Gaul, W. S. J. Rees, *Adv. Mater.* **2000**, *12*, 935.
[9] G. Chen, M. Craven, A. Kim, A. Munkholm, S. Watanabe, M. Camras, W. Gotz, F. Steranka, *Phys. Status Solidi A* **2008**, *205*, 1086.
[10] R. Meerheim, S. Scholz, S. Olthof, G. Schwartz, S. Reineke, K. Walzer, K. Leo, *J. Appl. Phys.* **2008**, *104*, 014510.
[11] E. F. Schubert, J. K. Kim, *Science* **2005**, *308*, 1274.
[12] a) A. Carlson, A. M. Bowen, Y. Huang, R. G. Nuzzo, J. A. Rogers, *Adv. Mater.* **2012**, *24*, 5284; b) D. Akinwande, N. Petrone, J. Hone, *Nat. Commun.* **2014**, *5*, 5678; c) J. Yoon, S.-M. Lee, D. Kang, M. Meitl, A. M. Bowen, J. A. Rogers, *Adv. Opt. Mater.* **2015**, *3*, 1313; d) J. Yoon, A. J. Baca, S.-I. Park, P. Elvikis, J. B. Geddes, L. S. Li, R. H. Kim, J. Xiao, S. Wang, T.-H. Kim, M. J. Motala,

B. Y. Ahn, E. B. Duoss, J. A. Lewis, R. G. Nuzzo, P. M. Ferreira, Y. Huang, A. Rockett, J. A. Rogers, *Nat. Mater.* **2008**, *7*, 907; e) J. He, R. G. Nuzzo, J. A. Rogers, *Proc. IEEE* **2015**, *103*, 619.

[13] a) J. Yoon, S. Jo, I. S. Chun, I. Jung, H.-S. Kim, M. Meitl, E. Menard, X. Li, J. J. Coleman, U. Paik, J. A. Rogers, *Nature* **2010**, *465*, 329; b) S.-I. Park, A.-P. Le, J. Wu, Y. Huang, X. Li, J. A. Rogers, *Adv. Mater.* **2010**, *22*, 3062; c) R.-H. Kim, D.-H. Kim, J. Xiao, B. H. Kim, S.-I. Park, B. Panilaitis, R. Ghaffari, J. Yao, M. Li, Z. Liu, V. Malyarchuk, D. G. Kim, A.-P. Le, R. G. Nuzzo, D. L. Kaplan, F. G. Omenetto, Y. Huang, Z. Kang, J. A. Rogers, *Nat. Mater.* **2010**, *9*, 929; d) D.-H. Kim, N. Lu, R. Ghaffari, Y.-S. Kim, S. P. Lee, L. Xu, J. Wu, R.-H. Kim, J. Song, Z. Liu, J. Viventi, B. De Graff, B. Elolampi, M. Mansour, M. J. Slepian, S. Hwang, J. D. Moss, S.-M. Won, Y. Huang, B. Litt, J. A. Rogers, *Nat. Mater.* **2011**, *10*, 316; e) D.-H. Kim, N. Lu, Y. Huang, J. A. Rogers, *MRS Bull.* **2012**, *37*, 226; f) H.-S. Kim, E. Brueckner, J. Song, Y. Li, S. Kim, C. Lu, J. Sulkin, K. Choquette, Y. Huang, R. G. Nuzzo, J. A. Rogers, *Proc. Natl. Acad. Sci. USA* **2011**, *108*, 10072; g) R.-H. Kim, H. Tao, T.-I. Kim, Y. Zhang, S. Kim, B. Panilaitis, M. Yang, D.-H. Kim, Y. H. Jung, B. H. Kim, Y. Li, Y. Huang, F. G. Omenetto, J. A. Rogers, *Small* **2012**, *8*, 2812; h) T.-I. Kim, Y. H. Jung, J. Song, D. Kim, Y. Li, H.-S. Kim, I.-S. Song, J. J. Wierer, H. A. Pao, Y. Huang, J. A. Rogers, *Small* **2012**, *8*, 1643; i) R.-H. Kim, S. Kim, Y. M. Song, H. Jeong, T.-I. Kim, J. Lee, X. Li, K. Choquette, J. A. Rogers, *Small* **2012**, *8*, 3123; j) T.-I. Kim, J. G. McCall, Y. H. Jung, X. Huang, E. R. Siuda, Y. Li, J. Song, Y. M. Song, H. A. Pao, R.-H. Kim, C. Lu, S. D. Lee, I.-S. Song, G. Shin, R. Al-Hasani, S. Kim, M. P. Tan, Y. Huang, F. G. Omenetto, J. A. Rogers, M. R. Bruchas, *Science* **2013**, *340*, 211; k) J.-W. Jeong, J. G. McCall, G. Shin, Y. Zhang, R. Al-Hasani, M. Kim, S. Li, J. Y. Sim, K.-I. Jang, Y. Shi, D. Y. Hong, Y. Liu, G. P. Schmitz, L. Xia, Z. He, P. Gamble, W. Z. Ray, Y. Huang, M. R. Bruchas, J. A. Rogers, *Cell* **2015**, *162*, 662; l) S. I. Park, G. Shin, A. Banks, J. G. McCall, E. R. Siuda, M. J. Schmidt, H. U. Chung, K. N. Noh, J. G.-H. Mun, J. Rhodes, M. R. Bruchas, J. A. Rogers, *J. Neural Eng.* **2015**, *12*, 056002.

[14] a) T.-I. Kim, Y. H. Jung, H.-J. Chung, K. J. Yu, N. Ahmed, C. Corcoran, J. S. Park, S. H. Jin, J. A. Rogers, *Appl. Phys. Lett.* **2012**, *110*, 253104; b) T.-I. Kim, M. J. Kim, Y. H. Jung, H. W. Jang, C. Dagdeviren, H. A. Pao, S. J. Cho, A. Carlson, K. J. Yu, A. Ameen, H.-J. Chung, S. H. Jin, Z. Ma, J. A. Rogers, *Chem. Mater.* **2014**, *26*, 3502.

[15] R.-H. Kim, M.-H. Bae, D. G. Kim, H. Cheng, B. H. Kim, D.-H. Kim, M. Li, J. Wu, F. Du, H.-S. Kim, S. Kim, D. Estrada, S. W. Hong, Y. Huang, E. Pop, J. A. Rogers, *Nano Lett.* **2011**, *11*, 3881.

[16] D.-H. Kim, J.-H. Ahn, W. M. Choi, H.-S. Kim, T.-H. Kim, J. Song, Y. Huang, Z. Liu, C. Lu, J. A. Rogers, *Science* **2008**, *320*, 507.

[17] J. Y. Tsao, M. E. Coltrin, M. H. Crawford, J. A. Simmons, *Proc. IEEE* **2010**, *98*, 1162.

[18] J.-H. Seo, J. Li, J. Lee, S. Gong, J. Lin, H. Jiang, Z. Ma, *IEEE Photonics J.* **2015**, *7*, 8200207.

[19] S. Y. Lee, K.-I. Park, C. Huh, M. Koo, H. G. Yoom, S. Kim, C.-S. Ah, G. Y. Sung, K. J. Lee, *Nano Energy* **2012**, *1*, 145.

[20] a) J. G. McCall, T.-I. Kim, G. Shin, X. Huang, Y. H. Jung, R. Al-Hasani, F. G. Omenetto, M. R. Bruchas, J. A. Rogers, *Nat. Protoc.* **2013**, *8*, 2413; b) Y. Jung, X. Wang, J. Kim, S. H. Kim, F. Ren, S. Pearton, J. Kim, *Appl. Phys. Lett.* **2012**, *100*, 231113.

[21] a) A. J. Baca, M. Meitl, H. C. Ko, S. Mack, H.-S. Kim, J. Dong, P. M. Ferreira, J. A. Rogers, *Adv. Funct. Mater.* **2007**, *17*, 3051; b) K. E. Bean, *IEEE Trans. Electron Devices* **1978**, *ED-25*, 1185.

[22] S. H. Park, G. Yuan, D. Chen, K. Xiong, J. Song, B. Leung, J. Han, *Nano Lett.* **2014**, *14*, 4293.

[23] M. Konagai, M. Sugimoto, K. Takahashi, *J. Cryst. Growth* **1978**, *45*, 277.

[24] a) K. Chung, H. Yoo, J. K. Hyun, H. Oh, Y. Tchoe, K. Lee, H. Baek, M. Kim, G.-C. Yi, *Adv. Mater.* **2016**, *28*, 7688; b) K. Y. Zang, D. W. C. Cheong, H. F. Liu, H. Liu, J. H. Teng, S. J. Chua, *Nanoscale Res. Lett.* **2010**, *5*, 1051; c) Y. Sun, R. A. Graff, M. S. Strano, J. A. Rogers, *Small* **2005**, *1*, 1052; d) K. J. Lee, J. Lee, H. Hwang, Z. J. Reitmeier, R. F. Davis, J. A. Rogers, R. G. Nuzzo, *Small* **2005**, *1*, 1164; e) C. Lee, Y.-J. Kim, Y. J. Hong, S.-R. Jeon, S. Bae, B. H. Hong, G.-C. Yi, *Adv. Mater.* **2011**, *23*, 4614.

[25] a) K. Chung, C. Lee, G.-C. Yi, *Science* **2010**, *330*, 655; b) Y. Kim, S. S. Cruz, K. Lee, B. O. Alawode, C. Choi, Y. Song, J. M. Johnson, C. Heidelberger, W. Kong, S. Choi, K. Qiao, I. Almansouri, E. A. Fitzgerald, J. Kong, A. M. Kolpak, J. Hwang, J. Kim, *Nature* **2017**, *544*, 340.

[26] a) X. Dai, A. Messanvi, H. Zhang, C. Durand, J. Eymery, C. Bougerol, F. H. Julien, M. Tchernycheva, *Nano Lett.* **2015**, *15*, 6958; b) N. Guan, X. Dai, A. Messanvi, H. Zhang, J. Yan, E. Gautier, C. Bougerol, F. H. Julien, C. Durand, J. Eymery, M. Tchernycheva, *ACS Photonics* **2016**, *3*, 597; c) N. D. Guan, X. A. V. Babichev, F. H. Julien, M. Tchernycheva, *Chem. Sci.* **2017**, *8*, 7904.

[27] a) C. K. Jeong, K.-I. Park, J. H. Son, G.-T. Hwang, S. H. Lee, D. Y. Park, H. E. Lee, H. K. Lee, M. Byun, K. J. Lee, *Energy Environ. Sci.* **2014**, *7*, 4035; b) S. H. Lee, J. Kim, J. H. Shin, H. E. Lee, I.-S. Kang, K. Gwak, D.-S. Kim, D. Kim, K. J. Lee, *Nano Energy* **2018**, *44*, 447.

[28] S.-M. Moon, J. S. Kwak, *J. Korean Phys. Soc.* **2009**, *55*, 1128.

[29] D. V. Talapin, J.-S. Lee, M. V. Kovalenko, E. V. Shevchenko, *Chem. Rev.* **2010**, *110*, 389.

[30] M. A. Boles, D. Ling, T. Hyeon, D. V. Talapin, *Nat. Mater.* **2014**, *15*, 141.

[31] a) V. L. Colvin, M. C. Schlamp, A. P. Alivisatos, *Nature* **1994**, *370*, 354; b) S. Coe, W.-K. Woo, M. G. Bawendi, V. Bulovic, *Nature* **2002**, *420*, 800.

[32] a) M. K. Choi, J. Yang, T. Hyeon, D.-H. Kim, *npj Flexible Electron.* **2018**, *2*, 10; b) D. V. Talapin, J. Steckel, *MRS Bull.* **2013**, *38*, 685.

[33] A. L. Rogach, D. V. Talapin, E. V. Shevchenko, A. Kornowski, M. Haase, H. Weller, *Adv. Funct. Mater.* **2002**, *12*, 653.

[34] J. Lim, Y.-S. Park, V. I. Klimov, *Nat. Mater.* **2018**, *17*, 42.

[35] N. Oh, S. Nam, Y. Zhai, K. Deshpande, P. Trefonas, M. Shim, *Nat. Commun.* **2014**, *5*, 3642.

[36] a) C. R. Kagan, E. Lifshitz, E. H. Sargent, D. V. Talapin, *Science* **2016**, *353*, aac5523; b) C. R. Kagan, C. B. Murray, *Nat. Nanotechnol.* **2015**, *10*, 1013; c) H. Goesmann, C. Feldmann, *Angew. Chem., Int. Ed.* **2009**, *49*, 1362.

[37] C. B. Murray, D. J. Norris, M. G. Bawendi, *J. Am. Chem. Soc.* **1993**, *115*, 8706.

[38] a) D. V. Talapin, C. B. Murray, *Science* **2005**, *310*, 86; b) M. A. Hines, G. D. Scholes, *Adv. Mater.* **2003**, *15*, 1844.

[39] a) O. I. Micic, C. J. Curtis, K. M. Jones, J. R. Sprague, A. J. Nozik, *J. Phys. Chem. B* **2005**, *109*, 18243; b) D. V. Talapin, A. L. Rogach, E. V. Shevchenko, A. Kornowski, M. Haase, H. Weller, *J. Am. Chem. Soc.* **2002**, *124*, 5782.

[40] J. Cui, A. P. Beyler, I. Coropceanu, L. Cleary, T. R. Avila, Y. Chen, J. M. Cordero, S. L. Heathcote, D. K. Harris, O. Chen, J. Cao, M. G. Bawendi, *Nano Lett.* **2016**, *16*, 289.

[41] a) M. A. Hines, P. Guyot-Sionnest, *J. Phys. Chem.* **1996**, *100*, 468; b) B. N. Pal, Y. Ghosh, S. Brovelli, R. Laocharoensuk, V. I. Klimov, J. A. Hollingsworth, H. Htoon, *Nano Lett.* **2011**, *12*, 331.

[42] a) C. Pu, X. Peng, *J. Am. Chem. Soc.* **2016**, *138*, 8134; b) A. B. Greytak, P. M. Allen, W. Liu, J. Zhao, E. R. Young, Z. Popovic, B. J. Walker, D. G. Nocera, M. G. Bawendi, *Chem. Sci.* **2012**, *3*, 2028.

[43] a) S. Nam, N. Oh, Y. Zhao, M. Shim, *ACS Nano* **2015**, *9*, 878; b) N. Oh, B. H. Kim, S.-Y. Cho, S. Nam, S. P. Rogers, Y. Jiang, J. C. Flanagan, Y. Zhai, J.-H. Kim, J. Lee, Y. Yu, Y. K. Cho, G. Hur, J. Zhang, P. Trefonas, J. A. Rogers, M. Shim, *Science* **2017**, *355*, 616.

[44] X. Dai, Z. Zhang, Y. Jin, Y. Niu, H. Cao, X. Liang, L. Chen, J. Wang, X. Peng, *Nature* **2014**, *515*, 96.

[45] J. Lim, B. Jeong, M. Park, J. K. Kim, J. M. Pietryga, Y.-S. Park, V. I. Klimov, C. Lee, D. C. Lee, W. K. Bae, *Adv. Mater.* **2014**, *26*, 8034.
[46] D. Kim, Y. Fu, S. Kim, W. Lee, K.-H. Lee, H. K. Chung, H.-J. Lee, H. Yang, H. Chae, *ACS Nano* **2017**, *11*, 1982.
[47] J. Kwak, W. K. Bae, D. C. Lee, L. Park, J. Lim, M. Park, H. Cho, H. Woo, D. Y. Yoon, K. Char, C. Lee, S. Lee, *Nano Lett.* **2012**, *12*, 2362.
[48] a) Y. Yang, Y. Zheng, W. cao, A. Titov, J. Hyvonen, R. Mandersjesse, J. Xue, P. H. Holloway, L. Qian, *Nat. Photonics* **2015**, *9*, 259; b) H. Shen, W. Cao, N. T. Shewmon, C. Yang, L. S. Li, J. Xue, *Nano Lett.* **2015**, *15*, 1211.
[49] a) T.-H. Kim, D.-Y. Chung, J. Ku, I.-S. Song, S. Sul, D.-Y. Kim, K.-S. Cho, B. L. Choi, J. M. Kim, S. Hwang, K. Kim, *Nat. Commun.* **2013**, *4*, 2637; b) M. K. Choi, J. Yang, K. Kang, D. C. Kim, C. Choi, C. Park, S. J. Kim, S. I. Chae, T.-H. Kim, J. H. Kim, T. Hyeon, D.-H. Kim, *Nat. Commun.* **2015**, *6*, 7149; c) B. H. Kim, S. Nam, N. Oh, S.-Y. Cho, K. J. Yu, C. H. Lee, J. Zhang, K. Deshpande, P. Trefonas, J.-H. Kim, J. Lee, J. H. Shin, Y. Yu, J. B. Lim, S.-M. Won, Y. K. Cho, N. H. Kim, K. J. Seo, H. E. Lee, T. I. Kim, H. J. Shim, J. A. Rogers, *ACS Nano* **2016**, *10*, 4920; d) L. Kim, P. Anikeeva, S. A. Coe-Sullivan, J. Steckel, M. G. Bawendi, V. Bulovic, *Nano Lett.* **2008**, *8*, 4513.
[50] T.-H. Kim, K.-S. Cho, E. K. Lee, S. J. Lee, J. Chae, J. W. Kim, D. H. Kim, J.-Y. Kwon, G. Amaratunga, S. Y. Lee, B. L. Choi, Y. Kuk, J. M. Kim, K. Kim, *Nat. Photonics* **2011**, *5*, 176.
[51] B. H. Kim, M. S. Onses, J. B. Lim, S. Nam, N. Oh, H.-S. Kim, K. J. Yu, J. W. Lee, J.-H. Kim, S.-K. Kang, C. H. Lee, J. Lee, J. H. Shin, N. H. Kim, C. Leal, M. Shim, J. A. Rogers, *Nano Lett.* **2015**, *15*, 969.
[52] Y. Wang, I. Fedin, H. Zhang, D. V. Talapin, *Science* **2017**, *357*, 385.
[53] T.-H. Kim, C.-S. Lee, S. Kim, J. Hur, S. Lee, K. W. Shin, Y.-Z. Yoon, M. K. Choi, J. Yang, D.-H. Kim, T. Hyeon, S.-I. Park, S. Hwang, *ACS Nano* **2017**, *11*, 5992.
[54] V. Wood, M. J. Panzer, J. Chen, M. S. Bradley, J. E. Halpert, M. G. Bawendi, V. Bulovic, *Adv. Mater.* **2009**, *21*, 2151.
[55] Y. L. Kong, I. A. Tamargo, H. Kim, B. N. Johnson, M. K. Gupta, T.-W. Koh, H.-A. Chin, D. A. Steingart, B. P. Rand, M. C. McAlpine, *Nano Lett.* **2014**, *14*, 7017.
[56] a) M. K. Choi, J. Yang, D. C. Kim, Z. Dai, J. Kim, H. Seung, V. S. Kale, S. J. Sung, C. R. Park, N. Lu, T. Hyeon, D.-H. Kim, *Adv. Mater.* **2018**, *30*, 1703279; b) J.-K. Song, D. Son, J. Kim, Y. J. Yoo, G. J. Lee, L. Wang, M. K. Choi, J. Yang, M. Lee, K. Do, J. H. Koo, N. Lu, J. H. Kim, T. Hyeon, Y. M. Song, D.-H. Kim, *Adv. Funct. Mater.* **2016**, *27*, 1605286; c) J. Kim, H. J. Shim, J. Yang, M. K. Choi, D. C. Kim, J. Kim, T. Hyeon, D.-H. Kim, *Adv. Mater.* **2017**, *29*, 1700217.
[57] W. K. Bae, J. Lim, D. Lee, M. Park, H. Lee, J. Kwak, K. Char, C. Lee, S. Lee, *Adv. Mater.* **2014**, *26*, 6387.
[58] X. Yang, E. Mutlugun, C. Dang, K. Dev, Y. Gao, S. T. Tan, X. W. Sun, H. V. Demir, *ACS Nano* **2014**, *8*, 8224.
[59] D. Son, S. I. Chae, M. Kim, M. K. Choi, J. Yang, K. Park, V. S. Kale, J. H. Koo, C. Choi, M. Lee, J. H. Kim, T. Hyeon, D.-H. Kim, *Adv. Mater.* **2016**, *28*, 9326.
[60] N.-G. Park, M. Gratzel, T. Miyasaka, K. Zhu, K. Emery, *Nat. Energy* **2016**, *1*, 16152.
[61] NREL, in *Efficiency Chart*, https://www.nrel.gov/pv/assets/images/efficiency-chart-20180716.jpg (accessed: July 2018).
[62] O. D. Miller, E. Yablonovitch, S. R. Kurtz, *IEEE J. Photovoltaics* **2012**, *2*, 303.
[63] a) Z.-K. Tan, R. S. Moghaddam, M. L. Lai, P. Docampo, R. Higler, F. Deschler, M. Price, A. Sadhanala, L. M. Pazos, D. Credgington, F. Hanusch, T. Bein, H. J. Snaith, R. H. Friend, *Nat. Nanotechnol.* **2014**, *9*, 687; b) Y.-H. Kim, H. Cho, J. H. Heo, T.-S. Kim, N. Myoung, C.-L. lee, S. H. Im, T.-W. Lee, *Adv. Mater.* **2014**, *27*, 1248.
[64] a) M. V. Kovalenko, L. Protesecu, M. I. Bodnarchuk, *Science* **2017**, *358*, 745; b) L. Protesecu, S. Yakunin, M. I. Bodnarchuk, F. Kreig, R. Caputo, C. H. Hendon, R. X. Yang, A. Walsh, M. V. Kovalenko, *Nano Lett.* **2015**, *15*, 3692.
[65] D. Zhang, S. W. Eaton, Y. Yu, L. Dou, P. Yang, *J. Am. Chem. Soc.* **2015**, *137*, 9230.
[66] Y. Bekenstin, B. A. Koscher, S. W. Eaton, P. Yang, A. P. Alivisatos, *J. Am. Chem. Soc.* **2015**, *137*, 16008.
[67] a) W. Zhang, G. E. Eperon, H. J. Snaith, *Nat. Energy* **2016**, *1*, 16048; b) N. J. Jeon, J. H. Noh, Y. C. Kim, W. S. Yang, S. Ryu, S. I. Seok, *Nat. Mater.* **2014**, *13*, 897.
[68] M. I. Saidaminov, A. L. Abdelhady, B. Murali, E. Alarousu, V. M. Burlakov, W. Peng, I. Dursun, L. Wang, Y. He, G. Maculan, A. Goriely, T. Wu, O. F. Mohammed, O. M. Bakr, *Nat. Commun.* **2015**, *6*, 7586.
[69] a) N. Wang, L. Cheng, R. Ge, S. Zhang, Y. Miao, W. Zou, C. Yi, Y. Sun, Y. Cao, R. Yang, Y. Wei, Q. Guo, Y. Ke, M. Yu, Y. Jin, Y. Liu, Q. Ding, D. Di, L. Yang, G. Xing, H. Tian, C. Jin, F. Gao, R. H. Friend, J. Wang, W. Huang, *Nat. Photonics* **2016**, *10*, 699; b) X. Yang, X. Zhang, J. Deng, Z. Chu, Q. Jiang, J. Meng, P. Wang, L. Zhang, Z. Yin, J. You, *Nat. Commun.* **2018**, *9*, 570.
[70] H. Cho, S.-H. Jeong, M.-H. Park, Y.-H. Kim, C. Wolf, C.-L. Lee, J. H. Heo, A. Sadhanala, N. Myoung, S. Yoo, S. H. Im, R. H. Friend, T.-W. Lee, *Science* **2015**, *350*, 1222.
[71] S. D. Stranks, G. E. Eperon, G. Grancini, C. Menelaou, M. J. P. Alcocer, T. Leijtens, L. M. Herz, A. Petrozza, H. J. Snaith, *Science* **2013**, *342*, 341.
[72] H.-K. Seo, H.-S. Kim, J. Lee, M.-H. Park, S.-H. Jeong, Y.-H. Kim, S.-J. Kwon, T.-H. Han, S. Yoo, T.-W. Lee, *Adv. Mater.* **2017**, *29*, 1605587.
[73] S. Kumar, J. Jagielski, N. Kallikounis, Y.-H. Kim, C. Wolf, F. Jenny, T. Tian, C. J. Hofer, Y.-C. Chiu, W. J. Stark, T.-W. Lee, C.-J. Shih, *Nano Lett.* **2017**, *17*, 5277.
[74] Y. Tong, E.-P. Yao, A. Manzi, E. Bladt, K. Wang, M. Doblinger, S. Bals, P. Muller-Buschbaum, A. S. Urban, L. Polavarapu, J. Feldmann, *Adv. Mater.* **2018**, *30*, 1801117.
[75] F. Zhao, D. Chen, S. Chang, H. Huang, K. Tong, C. Xiao, S. Chou, H. Zhong, Q. Pei, *J. Mater. Chem. C* **2017**, *5*, 531.
[76] a) M. Liu, M. B. Johnson, H. J. Snaith, *Nature* **2013**, *501*, 395; b) J. Avila, C. Momblona, P. P. Boix, M. Sessolo, H. J. Bolink, *Joule* **2017**, *1*, 431.
[77] Y.-H. Kim, S. Kim, S. H. Jo, T.-W. Lee, *Small Methods* **2018**, *113*, 1800093.
[78] a) M. R. Leyden, L. Meng, Y. Jiang, L. K. Ono, L. Qiu, E. J. Juarez-Perez, C. Qin, C. Adachi, Y. Qi, *J. Phys. Chem. Lett.* **2017**, *8*, 3193; b) H. Ji, Z. Shi, X. Sun, Y. Li, S. Li, L. Lei, D. Wu, T. Xu, X. Li, G. Du, *ACS Appl. Mater. Interfaces* **2017**, *9*, 42893.
[79] S. G. R. Bade, J. Li, X. Shan, Y. Ling, Y. Tian, T. Dilbeck, T. Besara, T. Geske, H. Gao, B. Ma, K. Hanson, T. Siegrist, C. Xu, Z. Yu, *ACS Nano* **2016**, *10*, 1795.
[80] A. Daus, C. Roldan-Carmona, K. Domanski, S. Knobelspies, G. Cantarella, C. Vogt, M. Gratzel, M. K. Nazeeruddin, G. Troster, *Adv. Mater.* **2018**, *30*, 1707412.
[81] Y. Liu, N. O. Weiss, X. Duan, H.-C. Cheng, Y. Huang, X. Duan, *Nat. Rev. Mater.* **2016**, *1*, 16042.
[82] W. Zhang, Q. Wang, Y. Chen, Z. Wang, A. T. S. Wee, *2D Mater.* **2016**, *3*, 022001.
[83] a) H. Kim, J.-H. Ahn, *Carbon* **2017**, *120*, 244; b) B. Radisavljevic, A. Rdenovic, J. Brivio, V. Giacometti, K. A. , *Nat. Nanotechnol.* **2011**, *6*, 147; c) B. Radisavljevic, A. Kis, *Nat. Mater.* **2013**, *12*, 815; d) L. Gao, *Small* **2017**, *13*, 1603994; e) K. F. Mak, J. Shan, *Nat. Photonics* **2016**, *10*, 216; f) O. Lopez-Sanchez, D. Lembke, M. Kayci, A. Radenovic, A. Kis, *Nat. Nanotechnol.* **2013**, *8*, 497.
[84] a) M. K. Choi, Y. J. Park, B. K. Sharma, S.-R. Bae, S. Y. Kim, J.-H. Ahn, *Sci. Adv.* **2018**, *4*, eaas8721; b) G. J. Choi, Q. V. Le,

K. S. Choi, K. C. Kwon, H. W. Jang, J. S. Gwag, S. Y. Kim, *Adv. Mater.* **2017**, *29*, 1702598; c) X. Zhou, X. Hu, J. Yu, S. Liu, Z. Shu, Q. Zhang, H. Li, Y. Ma, H. Xu, T. Zhai, *Adv. Funct. Mater.* **2018**, *28*, 1706587.

[85] D.-H. Lien, M. Amani, S. B. Desai, G. H. Ahn, K. Han, J.-H. He, J. W. I. Ager, M. C. Wu, A. Javey, *Nat. Commun.* **2016**, *9*, 1229.

[86] H. Kim, D.-H. Lien, M. Amani, J. W. I. Ager, A. Javey, *ACS Nano* **2017**, *11*, 5179.

[87] M. Amani, D.-H. Lien, D. Kiriya, J. Xiao, A. Azcatl, J. Noh, S. R. Madhvapathy, R. Addou, S. KC, M. Dubey, K.-S. Cho, R. M. Wallace, S.-C. Lee, J.-H. He, J. W. I. Ager, X. Zhang, E. Yablonovitch, A. Javey, *Science* **2015**, *350*, 1065.

[88] R. S. Sundaram, M. Engel, A. Lombardo, R. Krupke, A. C. Ferrari, P. Avouris, M. Steiner, *Nano Lett.* **2013**, *13*, 1416.

[89] a) R. Cheng, D. Li, H. Zhou, C. Wang, A. Yin, S. Jiang, Y. Liu, Y. Chen, Y. Huang, X. Duan, *Nano Lett.* **2014**, *14*, 5990; b) O. Lopez-Sanchez, E. A. Llado, V. Koman, A. F. I. Morral, A. Radenovic, A. Kis, *ACS Nano* **2014**, *8*, 3042; c) J. S. Ross, P. Klement, A. M. Jones, N. J. Ghimire, J. Yan, D. G. Mandrus, T. Taniguchi, K. Watanabe, K. Kitamura, W. Yao, D. H. Cobden, X. Xu, *Nat. Nanotechnol.* **2014**, *9*, 268; d) B. W. H. Baugher, H. O. H. Churchill, Y. Yang, P. Jarillo-Herreo, *Nat. Nanotechnol.* **2014**, *9*, 262.

[90] a) F. Withers, O. Del Pozo-Zamudio, A. Mishchenko, A. P. Rooney, A. Gholinia, K. Watanabe, T. Taniguchi, S. J. Haigh, A. K. Geim, A. I. Tartakovskii, K. S. Novoselov, *Nat. Mater.* **2015**, *14*, 301; b) G. Palacios-Berraquero, M. Barbone, D. M. Kara, X. Chen, I. Goykhman, D. Yoon, A. K. Ott, J. Bietner, K. Watanabe, T. Taniguchi, A. C. Ferrari, M. Atature, *Nat. Commun.* **2016**, *7*, 12978.

[91] X. Wang, H. Tian, M. A. Mohammad, C. Li, C. Wu, Y. Yang, T.-L. Ren, *Nat. Commun.* **2015**, *6*, 7767.

[92] a) W. Kwon, Y.-H. Kim, C.-L. Lee, M. Lee, H. C. Choi, T.-W. Lee, S.-W. Rhee, *ACS Nano* **2014**, *14*, 1306; b) S. H. Song, M.-H. Jang, J. Chuang, S. H. Jin, B. H. Kim, S.-H. Hur, S. Yoo, Y. H. Cho, S. Jeon, *Adv. Opt. Mater.* **2014**, *2*, 1016.

[93] a) F. Liu, M.-H. Jang, H. D. Ha, J.-H. Kim, Y.-H. Cho, T. S. Seo, *Adv. Mater.* **2013**, *25*, 3657; b) C. T. Chien, S. S. Li, W. J. Lai, Y. C. Yeh, H. A. Chen, I. S. Chen, L. C. Chen, K. H. Chen, T. Nemoto, S. Isoda, M. Chen, T. Fujita, G. Eda, H. Yamaguchi, M. Chhowalla, C. W. Chen, *Angew. Chem., Int. Ed.* **2012**, *51*, 6662; c) H. Yoon, Y. H. Chang, S. H. Song, E.-S. lee, S. H. Jin, C. Park, J. Lee, B. H. Kim, H. J. Kang, Y.-H. Kim, S. Jeon, *Adv. Mater.* **2016**, *28*, 5255; d) M.-H. Jang, S. H. Song, H. D. Ha, T. S. Seo, S. Jeon, Y.-H. Cho, *Carbon* **2017**, *118*, 524.

[94] D. McManus, S. Vranic, F. Withers, V. Sanchez-Romaguera, M. Macucci, H. Yang, R. Sorrentino, K. Rarvez, S.-K. Son, G. Iannaccone, K. Kostarelos, G. Fiori, C. Casiraghi, *Nat. Nanotechnol.* **2017**, *12*, 343.

[95] P. Gutruf, J. A. Rogers, *Curr. Opin. Neurobiol.* **2018**, *50*, 42.

[96] R. S. Cok, M. Meitl, R. Rotzoll, G. Melnik, A. Fecioru, A. J. Trindade, B. Raymond, S. Bonafede, D. Gomez, T. Moore, C. Prevatte, E. Radauscher, S. Goodwin, P. Hines, C. A. Bower, *J. Soc. Inf. Disp.* **2017**, *25*, 589.

[97] a) S.-M. Won, E. Song, J. Zhao, J. Li, J. Rivnay, J. A. Rogers, *Adv. Mater.* **2018**, *30*, 1800534; b) H. Fang, J. Zhao, K. J. Yu, E. Song, A. B. Farimani, C.-H. Chiang, X. Jin, Y. Xue, D. Xu, W. Du, K. J. Seo, Y. Zhong, Z. Yang, S.-M. Won, G. Fang, S. W. Choi, S. Chaudhuri, Y. Huang, M. A. Alam, J. Viventi, N. R. Aluru, J. A. Rogers, *Proc. Nat. Acad. Sci. USA* **2016**, *113*, 11683; c) E. Song, Y. K. Lee, R. Li, J. Li, X. Jin, K. J. Yu, Z. Xie, H. Fang, Y. Zhong, H. Du, J. Zhang, G. Fang, Y. Kim, Y. Yoon, M. A. Alam, Y. Mei, Y. Huang, J. A. Rogers, *Adv. Funct. Mater.* **2017**, *28*, 1702284; d) J. Viventi, D.-H. Kim, L. Vigeland, E. S. Frechette, J. A. Blanco, Y. S. Kim, A. E. Avrin, V. R. Tiruvadi, S.-W. Huang, A. C. Vanleer, D. F. Wulsin, K. Davis, C. E. Gelber, L. Palmer, J. Van der Spiegel, J. Wu, J. Xiao, Y. Huang, D. Contreras, J. A. Rogers, B. Litt, *Nat. Neurosci.* **2011**, *14*, 1599.

[98] J. Akerboom, N. C. Calderón, L. Tian, S. Wabnig, M. Prigge, J. Tolö, A. Gordus, M. B. Orger, K. E. Severi, J. J. Macklin, *Front. Mol. Neurosci.* **2013**, *6*, 2.

[99] a) J.-W. Jeong, G. Shin, S. I. Park, K. J. Yu, L. Xu, J. A. Rogers, *Neuron* **2015**, *86*, 175; b) Y. Li, X. Shi, J. Song, C. Lü, T.-i. Kim, J. G. McCall, M. R. Bruchas, J. A. Rogers, Y. Huang, *Proc. R. Soc. London, Ser. A* **2013**, *469*, 20130142; c) L. Lu, P. Gutruf, L. Xia, D. L. Bhatti, X. Wang, A. Vazquez-Guardado, X. Ning, X. Shen, T. Sang, R. Ma, G. Pakeltis, G. Sobczak, H. Zhang, D.-O. Seo, M. Xue, L. Yin, D. Chanda, X. Sheng, M. R. Bruchas, J. A. Rogers, *Proc. Natl. Acad. Sci. USA* **2018**, *115*, E1374; d) S. I. Park, D. S. Brenner, G. Shin, C. D. Morgan, B. A. Copits, H. U. Chung, M. Y. Pullen, K. N. Noh, S. Davidson, S. J. Oh, J. Yoon, K.-I. Jang, V. K. Samineni, M. Norman, J. G. Grajales-Reyes, S. K. Vogt, S. S. Sundaram, K. M. Wilson, J. S. Ha, R. Xu, T. Pan, T.-I. Kim, Y. Huang, M. C. Montana, J. P. Golden, M. R. Bruchas, R. W. I. Gereau, J. A. Rogers, *Nat. Biotechnol.* **2015**, *33*, 1280; e) S. I. Park, G. Shin, J. G. McCall, R. Al-Hasani, A. Norris, L. Xia, D. S. Brenner, K. N. Noh, S. Y. Bang, D. L. Bhatti, K.-I. Jang, S.-K. Kang, A. D. Mickle, G. Dussor, T. J. Price, R. W. I. Gereau, M. R. Bruchas, J. A. Rogers, *Proc. Natl. Acad. Sci. USA* **2016**, *113*, E8169; f) G. Shin, A. M. Gomez, R. Al-Hasani, Y. R. Jeong, J. Kim, Z. Xie, A. Banks, S. M. Lee, S. Y. Han, C. J. Yoo, J. L. Lee, S. H. Lee, J. Kurniawan, J. Tureb, Z. Guo, J. Yoon, S. I. Park, S. Y. Bang, Y. Nam, M. C. Walicki, V. K. Samineni, A. D. Mickle, K. Lee, S. Y. Heo, J. G. McCall, T. Pan, L.-P. Wang, X. Feng, T.-I. Kim, J. K. Kim, Y. Li, Y. Huang, R. W. I. Gereau, J. S. Ha, M. R. Bruchas, J. A. Rogers, *Neuron* **2017**, *93*, 509.

[100] O. Yizhar, L. E. Fenno, T. J. Davidson, M. Mogri, K. Deisseroth, *Neuron* **2011**, *71*, 9.

[101] N. McAlinden, D. Massoubre, E. Richardson, E. Gu, S. Sakata, M. D. Dawson, K. Mathieson, *Opt. Lett.* **2013**, *38*, 992.

[102] S.-W. Hwang, H. Tao, D.-H. Kim, H. Cheng, J.-K. Song, E. Rill, M. A. Brenckle, B. Panilaitis, S. M. Won, Y.-S. Kim, K. J. Yu, A. Ameen, R. Li, Y. Su, M. Yang, D. L. Kaplan, M. R. Zakin, M. J. Slepian, Y. Huang, F. G. Omenetto, J. A. Rogers, *Science* **2012**, *337*, 1640.

[103] H. Ding, L. Lu, Z. Shi, D. Wang, L. Li, X. Li, Y. Ren, C. Liu, D. Cheng, H. Kim, N. C. Giebink, X. Wang, L. Yin, L. Zhao, M. Luo, X. Sheng, *Proc. Natl. Acad. Sci. USA* **2018**, *115*, 6632.